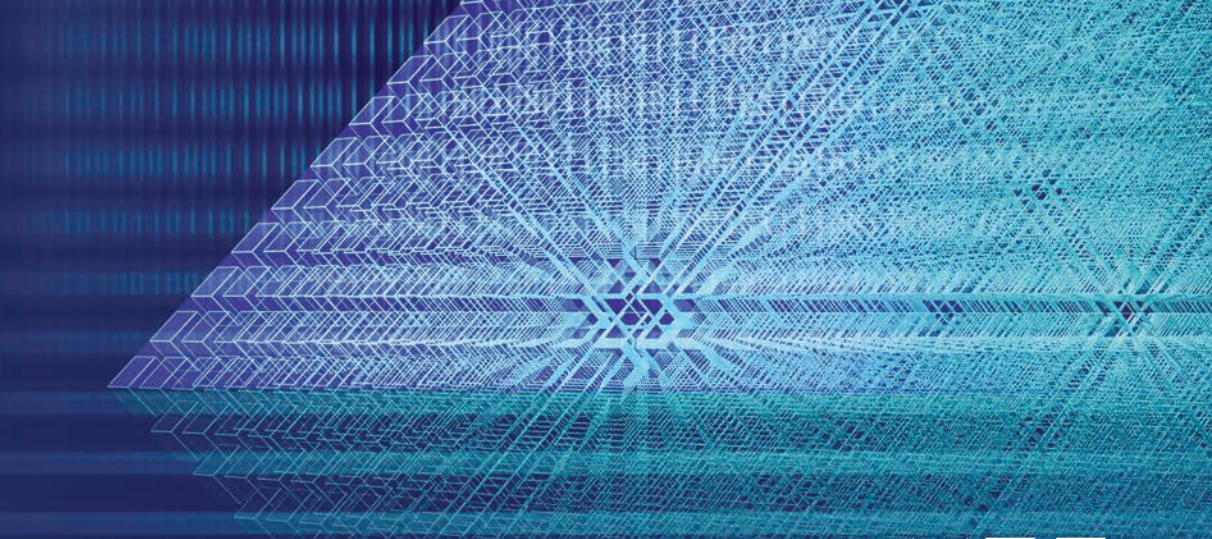

TECHNICAL REPORTS SERIES NO. 490

Guidelines for the Determination of Standardized Semiconductor Radiation Hardness Parameters

IAEA
International Atomic Energy Agency

GUIDELINES FOR THE DETERMINATION OF STANDARDIZED SEMICONDUCTOR RADIATION HARDNESS PARAMETERS

The following States are Members of the International Atomic Energy Agency:

AFGHANISTAN
ALBANIA
ALGERIA
ANGOLA
ANTIGUA AND BARBUDA
ARGENTINA
ARMENIA
AUSTRALIA
AUSTRIA
AZERBAIJAN
BAHAMAS
BAHRAIN
BANGLADESH
BARBADOS
BELARUS
BELGIUM
BELIZE
BENIN
BOLIVIA, PLURINATIONAL STATE OF
BOSNIA AND HERZEGOVINA
BOTSWANA
BRAZIL
BRUNEI DARUSSALAM
BULGARIA
BURKINA FASO
BURUNDI
CAMBODIA
CAMEROON
CANADA
CENTRAL AFRICAN REPUBLIC
CHAD
CHILE
CHINA
COLOMBIA
COMOROS
CONGO
COSTA RICA
CÔTE D'IVOIRE
CROATIA
CUBA
CYPRUS
CZECH REPUBLIC
DEMOCRATIC REPUBLIC OF THE CONGO
DENMARK
DJIBOUTI
DOMINICA
DOMINICAN REPUBLIC
ECUADOR
EGYPT
EL SALVADOR
ERITREA
ESTONIA
ESWATINI
ETHIOPIA
FIJI
FINLAND
FRANCE
GABON
GEORGIA
GERMANY
GHANA
GREECE
GRENADA
GUATEMALA
GUYANA
HAITI
HOLY SEE
HONDURAS
HUNGARY
ICELAND
INDIA
INDONESIA
IRAN, ISLAMIC REPUBLIC OF
IRAQ
IRELAND
ISRAEL
ITALY
JAMAICA
JAPAN
JORDAN
KAZAKHSTAN
KENYA
KOREA, REPUBLIC OF
KUWAIT
KYRGYZSTAN
LAO PEOPLE'S DEMOCRATIC REPUBLIC
LATVIA
LEBANON
LESOTHO
LIBERIA
LIBYA
LIECHTENSTEIN
LITHUANIA
LUXEMBOURG
MADAGASCAR
MALAWI
MALAYSIA
MALI
MALTA
MARSHALL ISLANDS
MAURITANIA
MAURITIUS
MEXICO
MONACO
MONGOLIA
MONTENEGRO
MOROCCO
MOZAMBIQUE
MYANMAR
NAMIBIA
NEPAL
NETHERLANDS
NEW ZEALAND
NICARAGUA
NIGER
NIGERIA
NORTH MACEDONIA
NORWAY
OMAN
PAKISTAN
PALAU
PANAMA
PAPUA NEW GUINEA
PARAGUAY
PERU
PHILIPPINES
POLAND
PORTUGAL
QATAR
REPUBLIC OF MOLDOVA
ROMANIA
RUSSIAN FEDERATION
RWANDA
SAINT KITTS AND NEVIS
SAINT LUCIA
SAINT VINCENT AND THE GRENADINES
SAMOA
SAN MARINO
SAUDI ARABIA
SENEGAL
SERBIA
SEYCHELLES
SIERRA LEONE
SINGAPORE
SLOVAKIA
SLOVENIA
SOUTH AFRICA
SPAIN
SRI LANKA
SUDAN
SWEDEN
SWITZERLAND
SYRIAN ARAB REPUBLIC
TAJIKISTAN
THAILAND
TOGO
TONGA
TRINIDAD AND TOBAGO
TUNISIA
TÜRKİYE
TURKMENISTAN
UGANDA
UKRAINE
UNITED ARAB EMIRATES
UNITED KINGDOM OF GREAT BRITAIN AND NORTHERN IRELAND
UNITED REPUBLIC OF TANZANIA
UNITED STATES OF AMERICA
URUGUAY
UZBEKISTAN
VANUATU
VENEZUELA, BOLIVARIAN REPUBLIC OF
VIET NAM
YEMEN
ZAMBIA
ZIMBABWE

The Agency's Statute was approved on 23 October 1956 by the Conference on the Statute of the IAEA held at United Nations Headquarters, New York; it entered into force on 29 July 1957. The Headquarters of the Agency are situated in Vienna. Its principal objective is "to accelerate and enlarge the contribution of atomic energy to peace, health and prosperity throughout the world".

TECHNICAL REPORTS SERIES No. 490

GUIDELINES FOR THE DETERMINATION OF STANDARDIZED SEMICONDUCTOR RADIATION HARDNESS PARAMETERS

INTERNATIONAL ATOMIC ENERGY AGENCY
VIENNA, 2023

COPYRIGHT NOTICE

Marketing and Sales Unit, Publishing Section
International Atomic Energy Agency
Vienna International Centre
PO Box 100
1400 Vienna, Austria
fax: +43 1 26007 22529
tel.: +43 1 2600 22417
email: sales.publications@iaea.org
www.iaea.org/publications

Printed by the IAEA in Austria
March 2023
STI/DOC/010/490

IAEA Library Cataloguing in Publication Data

Names: International Atomic Energy Agency.
Title: Guidelines for the determination of standardized semiconductor radiation hardness parameters / International Atomic Energy Agency.
Description: Vienna : International Atomic Energy Agency, 2023. | Series: Technical reports series, ISSN 0074–1914 ; no. 490 | Includes bibliographical references.
Identifiers: IAEAL 22-01562 | ISBN 978–92–0–100522–9 (paperback : alk. paper) | ISBN 978–92–0–122623–5 (pdf) | ISBN 978–92–0–100622–6 (epub)
Subjects: LCSH: Semiconductors — Radiation — Quality control. | Ionizing radiation. | Nuclear counters.
Classification: UDC 621.315.5 | STI/DOC/010/490

FOREWORD

Electronic devices containing semiconductor materials are used in harsh radiation environments in many fields of research and technology. High energy physics facilities, remote control systems in nuclear reactors, radiotherapy facilities and the aerospace sector are among the most significant areas where electronic devices are exposed to high levels of detrimental ionizing radiation.

The long term operating performance, reliability and lifetime of these electronic materials and devices are strictly related to their resistance to various types and levels of ionizing radiation, which induces a progressive degradation of their performance. The evaluation of the materials' radiation hardness (i.e. their resistance to accumulated damage caused by ionizing radiation) is crucial for the effective design of electronic devices. Therefore, reliable and widely applicable test methodologies suitable for determining radiation hardness (i.e. the measure of the non-vulnerability or of the resistance of the material to an accumulated level of radiation damage in a variety of experimental conditions) are needed to facilitate the optimal synthesis of materials for the design of electronic devices.

Ion accelerator based techniques provide insight into the phenomena underlying the formation of defects induced by energetic particles in semiconductor materials and their effects on the electronic features of the device. Because of the potential of these techniques, the IAEA implemented a coordinated research project from 2011 to 2016 entitled 'Utilization of Ion Accelerators for Studying and Modelling of Radiation Induced Defects in Semiconductors and Insulators' to investigate the mechanisms underlying the performance degradation of semiconductor devices induced by ionizing radiation. The objective of the project was to use accelerator based ion irradiation and analytical techniques to gain a deeper understanding of how different types of radiation influence the electronic properties of materials and devices, leading to an improved knowledge of radiation hardness and to the engineering of 'radiation harder' devices.

Research stimulated by the project resulted in publications in scientific journals, educational and scientific software packages, and a number of new collaborations among the participating research groups. The most significant outcomes of this project were the development of a protocol for existing experimental characterization techniques used to investigate radiation effects in semiconductor devices and the development of a relevant theoretical approach to interpret the experimental data.

This publication provides comprehensive guidelines for the assessment of the radiation hardness of semiconductor devices, including a detailed description of the experimental procedures, the theoretical model and the limits of its application, and data analysis techniques.

The intended audience includes professionals and technologists who wish to apply standardized practices in ion beam functional analysis of semiconductor materials. Solid state physicists and engineers involved in the design of electronic devices for use in harsh radiation environments might also benefit from using the theoretical model to obtain better predictions of the operating performance and lifetime of such devices.

The IAEA is grateful to E. Vittone of the University of Torino and all the other experts who contributed to this publication. The IAEA officer responsible for this publication was A. Simon of the Division of Physical and Chemical Sciences.

CONTENTS

1. INTRODUCTION 1

1.1. Background 1
1.2. Objective 3
1.3. Structure 4
1.4. Scope 4

2. MODELLING OF ELECTROSTATICS AND INDUCED CHARGE 6

2.1. Poisson and continuity equations in three dimensions 6
2.2. Determination of the dopant concentration profile 7
2.3. Electrostatics in one dimension under steady state conditions 9
2.4. Quasi-steady-state conditions 12
2.5. Modelling of the induced charge 14
2.6. The adjoint equation method for determining the induced charge 17

3. ENERGETIC ION–MATTER INTERACTIONS 20

3.1. Interaction mechanisms 20
3.2. Ion beam track parameters 21
3.3. Calculation of carrier and damage generation profiles using Monte Carlo simulations 23

4. EXPERIMENTAL PROCEDURES 25

4.1. Design of experimental procedures 25
4.2. Electronics and calibration 26
4.3. Ion microbeams 31

5. MODELLING OF THE CHARGE COLLECTION EFFICIENCY 41

5.1. Radiation induced carrier lifetime degradation 41
5.2. A general model for charge collection efficiency degradation in low damage conditions 43
5.3. Determination of the capture coefficients 53
5.4. Error budget 60

6. SUMMARY AND OUTLOOK 62

APPENDIX I: SUMMARY OF ASSUMPTIONS MADE IN THE MODEL. 67

APPENDIX II: FEATURES OF DEVICE UNDER STUDY 1. 68

APPENDIX III: FEATURES OF DEVICE UNDER STUDY 2. 69

APPENDIX IV: MOBILITY AND LIFETIME PARAMETERIZATION FOR SILICON. 72

APPENDIX V: DEVICE SIMULATION METHODS AND SOFTWARE. 73

REFERENCES 75
SYMBOLS 81
ABBREVIATIONS 87
CONTRIBUTORS TO DRAFTING AND REVIEW 89

1. INTRODUCTION

1.1. BACKGROUND

The operational lifetime of semiconductor devices working in harsh radiation environments is limited by the structural defects induced by the exposure to ionizing radiation. The long term accumulation of these defects can lead to a significant degradation of the devices' electronic performance. Therefore, a deep understanding of the types of defect formed and of their effects on the electronic properties of materials is of paramount importance for the development of new devices with improved radiation hardness.

Intensive studies have been carried out in different industrial contexts and by international scientific collaborations [1–3]. However, these tests are often tailored to specific problems (e.g. the certification procedure of devices for space applications) and their results are difficult to generalize to different devices and different irradiation conditions. Several studies have shown that the effects of different radiations could be correlated to the non-ionizing energy loss (NIEL) value [4–6], which has been found to be useful for characterizing displacement damage effects in electronic materials. The NIEL approach takes into account the creation of structural defects (vacancies) but does not consider their effect on the electrical properties of the semiconductor, whereas the degradation of the overall performance of the device depends on both the amount of radiation damage and on its operating conditions.

The radiation damage in a semiconductor device can be quantified by various physical observables, such as the power output, conductivity, lifetime and the charge collection efficiency (CCE), depending on the type of device. As an example [7, 8], Fig. 1 shows the performance degradation of a silicon diode expressed through the CCE. The left panel of Fig. 1 illustrates that the observed CCE degradation for damage introduced by the same ion type and energy depends on the bias conditions, whereas the right hand side of Fig. 1 demonstrates that for fixed applied bias voltage (i.e. fixed operating conditions), the CCE reduction with increasing fluence depends on the ion type and energy.

The need to develop a standardized procedure for the quantification of the radiation hardness of semiconductors that does not depend on operational parameters or irradiation details was addressed by IAEA's Coordinated Research Project F11016 (CRP F11016; 2011–2016), entitled Utilization of Ion Accelerators for Studying and Modelling of Radiation Induced Defects in Semiconductors and Insulators, which involved 14 institutions from 13 countries worldwide. CRP F11016 focused on semiconductor diodes and solid state ionization chambers, which can be used as detectors for ionizing radiation,

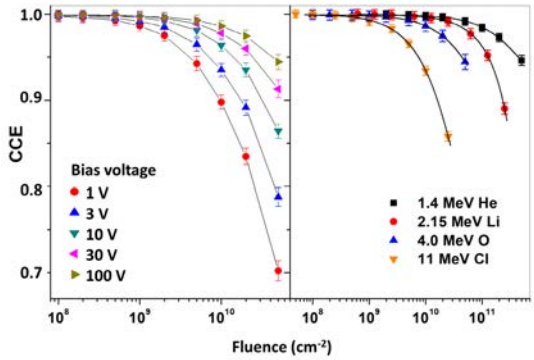

FIG. 1. Left: charge collection efficiency (CCE) degradation of a silicon diode at different bias voltages as a function of the fluence of 2 MeV He ions. Data from Refs [7, 8]. Right: CCE degradation of a silicon diode in full depletion conditions as a function of the fluence of ions with different masses and energies, probed by 1.4 MeV He. Data from Ref. [7].

including energetic ions. They represent examples of semiconductor devices with a simple geometry that are expected to undergo radiation induced modifications and damage implicit to their operation. In particular, the signal amplitude of these detectors is proportional to their CCE.

The following two main reasons motivated the choice of CCE as the most suitable physical observable to study radiation induced modification of the electronic properties of materials:

— The very high sensitivity of the CCE measurement to radiation damage, even at very low damage levels;
— The capability to use megaelectronvolt energy ions both as damaging and as probing tools on the same irradiation spot.

The permanent modifications of material properties analysed in this publication concern only modifications that manifest themselves in the electronic features of the material (i.e. mainly the increase of defect density and the subsequent decrease of carrier lifetime). They occur at a low level of damage, that is, they do not involve other effects such as changes in the transport (i.e. mobility) of charge carriers or in electrostatics (i.e. effective doping), which are typical for high level damage. Moreover, temporary changes (e.g. the creation of shallow traps, which can annihilate after annealing at room temperature) are not discussed in this publication.

For the cases studied, it has been proved that accurate knowledge of the electronic properties of a junction diode (i.e. electrode geometry, charge carrier

diffusion and drift mobilities, steady state charge carrier concentrations, dopant profiles and free charge carrier lifetimes) is sufficient to predict the CCE for all applied electric potentials and any type of probing beam used to generate the free charge carriers that are responsible for the signal.

For this publication, E. Vittone of the University of Torino integrated some of the research results published by the partners of CRP F11016, supported by additional material, to provide an exhaustive description of the experimental protocol, the theoretical model and the relevant limits of application, the data analysis procedure, and the physical observables that can be effectively measured and be used to assess the radiation hardness of semiconductor devices.

1.2. OBJECTIVE

In the development of guidelines for quantifying the radiation damage of semiconductor materials to predict their lifetime, the underlying principle is the measurement of the degradation of the charge collection efficiency as a function of ion beam induced radiation damage. The new, robust model presented here combines electrostatics with ion–matter interactions. This leads to the definition of a material parameter quantifying radiation hardness that is independent of the damaging beam and device geometry. The key novelty of this work is that this parameter enables the prediction of possible device performance degradation for previously untested operating and irradiation conditions. This work is expected to advance the understanding, and thus prediction, of the long term operating performance, reliability and lifetime of electronic devices under harsh radiation environments.

The objective of this publication is to establish material parameters that reflect semiconductor radiation hardness by predicting CCE degradation as a function of accumulated structural radiation damage.

In addition, the model detailed within this publication enables the prediction of the reduction in charge carrier lifetime, and hence the CCE, of ion beam damaged diodes for any damaging ion beam (DIB; i.e. any species, energy and fluence), using the electron and hole capture coefficients $\alpha_{e,h}$ within the range of parameters that fulfil the assumptions made in the model. Previously this had to be established in separate experiments for every ion type, energy and operational parameter.

Guidance provided here, describing good practices, represents expert opinion but does not constitute recommendations made on the basis of a consensus of Member States.

1.3. STRUCTURE

This report provides comprehensive guidelines for the determination of standardized parameters. Sections 2 and 3 introduce relevant concepts for semiconductor detector characterization and ion–matter interactions, respectively. Section 4 presents the experimental method, which is based on the ion beam induced charge (IBIC) technique [9]. The method can detect charge induced by the motion of free charge carriers generated by each ion within a rarefied (a few thousand ions per second) focused ion beam, illustrating that the technique is well suited in this context. The same experimental geometry, and frequently the same ions, are used both to damage the material under investigation and to detect the effects of the damage through the reduced signal produced by each subsequent ion. In addition, it is demonstrated that the analytical potential of this experimental method is further enhanced by the possibility of measuring the CCE degradation for different bias conditions of the diodes under study. The experimental technique and results of measurements for different ions and energies are presented for two different devices in Section 4. Section 5 details the robust theoretical formalism used for the modelling of IBIC experiments, which leads to the determination of $\alpha_{e,h}$. It builds on the fundamentals of electrostatics outlined in Section 2 and integrates the ionization and non-ionization ion energy loss in solids [10] (see Section 3). The refined theoretical model developed in CRP F11016 also incorporates the theory of charge induction in semiconductors [11, 12] and the electron–hole generation–recombination Shockley–Read–Hall model [13] to fully exploit the wealth of information contained in the CCE degradation curves obtained in different experimental conditions. Section 6 provides the summary and outlook. Detailed practical information with specific examples is given in Sections 2–6 on the experimental, theoretical and modelling steps to support knowledge transfer and implementation of the guidelines provided in this publication. The appendices provide details on the devices under study, the model and the simulation methods.

1.4. SCOPE

There are many publications in the literature that either compare CCE degradation (and hence some form of radiation hardness) in different semiconductors damaged with the same ionizing radiation energy and species (i.e. ion, electron or photon beams) or compare the performance degradation of one type of device (typically semiconductor radiation detector diodes) in different radiation fields; for examples (which are not related to CRP F11016 member groups), see Refs [14, 15].

There are two material properties that are predominantly used to quantitatively compare the quality of semiconductor bulk materials that is responsible for signal amplitude (and its degradation) in radiation detectors; these are the free charge carrier drift mobility $\mu_{e,h}$ for electrons (μ_e) and holes (μ_h) and the corresponding free electron and hole lifetimes $\tau_{e,h}$. These will be discussed in more detail in Section 2.

Low level radiation damage reduces the lifetimes of free charge carriers. This work interprets this reduction in terms of the parameters $\alpha_{e,h}$ (α_e for electrons and α_h for holes), which include both the capture cross-sections of traps generated by ion damage and the yield of electrically active traps generated by a single vacancy (the k factor), whose profile is predicted using SRIM[1] (Stopping and Range of Ions in Matter) Monte Carlo simulations [16].

This approach has the benefit of using a quantifiable measure of radiation hardness (within the range of parameters that fulfil the assumptions made in the model detailed in Section 5.2), $\alpha_{e,h}$, which is independent of the following:

— The ion species, energy and fluence used to induce the damage;
— The conditions used to probe the degradation of the performance of the semiconductor diode.

This report provides guidelines for determining $\alpha_{e,h}$ using planar diode semiconductor devices, which emerged from CRP F11016 as a development of the methodology proposed in Ref. [17] and Refs [7, 18], refined in both its experimental and theoretical aspects. The methodology relies on the validity of several assumptions, which constrain the device geometry and uniformity as well as the choice of experimental parameters, require sufficiently high quality charge transport calculations in the pristine (i.e. undamaged) materials and impose limitations on the mobility of the created defects. These assumptions are summarized in Appendix I.

The effectiveness of the guidelines was assessed and the interpretative model was validated through different types of ion beam irradiation and characterization. Most of the experimental data presented in this publication were acquired using a commercial silicon diode as a reference semiconducting material [8, 19, 20]. After the methodology was validated on silicon diodes, it was successfully applied to study radiation effects on other materials of high technological interest and with the potential of high radiation tolerance. These have been published elsewhere — see, for example, Refs [21, 22] for silicon carbide and Ref. [23] for diamond. An introduction to the methodology and some of the key results were published in a series of scientific papers in a special issue of Nuclear Instruments and Methods in Physics Research B [24].

[1] Available at www.srim.org

2. MODELLING OF ELECTROSTATICS AND INDUCED CHARGE

The physical observable that is investigated to determine the radiation damage in a semiconductor device is the CCE. The electrostatics of the device provides basic information for the evaluation of the CCE and is the focus of this section. The other inputs needed to model the radiation damage effects are the vacancy and ionization profiles of the ions, which are discussed in Section 3. In this section, the induced charge due to the motion of elementary charges within the device is described. Under the influence of an electric field, these charge carriers (electrons and holes) are driven to flow in opposite directions. An electric current occurring in a region within an electric field induces a current at the electrodes. The integral in time of the induced current provides the induced charge, which corresponds to the CCE if normalized by the amount of charge generated by ionization by the incident ion.

2.1. POISSON AND CONTINUITY EQUATIONS IN THREE DIMENSIONS

The fundamentals of charge transport of a semiconductor device are described by the continuity and Poisson equations; the change over time t in the carrier densities n (for electrons) and p (for holes) is the difference between the incoming and outgoing current fluxes plus the generation ($G_{e,h}$) and recombination ($R_{e,h}$) rates for the respective charge carriers. The continuity and Poisson equations are as follows:

$$\begin{cases} \dfrac{\partial n}{\partial t} = \nabla \cdot \left(D_e \nabla n - n \boldsymbol{v}_e \right) - R_e + G_e \\ \dfrac{\partial p}{\partial t} = \nabla \cdot \left(D_h \nabla p - p \boldsymbol{v}_h \right) - R_h + G_h \end{cases} \tag{1}$$

$$\nabla^2 \varphi = -\nabla \cdot \boldsymbol{E} = -\frac{\rho}{\varepsilon} = -\frac{q\left(N_D - N_A + p - n \right)}{\varepsilon} \tag{2}$$

where $\boldsymbol{v}_e$ ($\boldsymbol{v}_h$) is the drift velocity of the electrons (holes), D_e (D_h) is the diffusion coefficient of the electrons (holes), N_D (N_A) is the donor (acceptor) concentration, φ is the electrostatic potential, $\boldsymbol{E}$ is the electric field, q is the electron charge and ε is the dielectric permittivity of the material.

The solution of this system of differential equations provides the electron (n) and hole (p) concentrations, and hence the current density ($J_{e,h}$), the electrostatic potential and the electric field as functions of the semiconductor doping ($N_{D,A}$), of the carrier recombination mechanisms (described by $R_{e,h}$), of the transport parameters (i.e. mobility $\mu_{e,h}$ and diffusivity $D_{e,h}$), of the applied bias voltage and, in general, of the boundary and initial conditions.

2.2. DETERMINATION OF THE DOPANT CONCENTRATION PROFILE

The position dependent dopant concentration profiles within the dimensions of the device are used as inputs for the determination of the electrostatics of the diode, as seen in Eqs (1, 2), and subsequently for the evaluation of the charge carrier transport (mobility and lifetime) parameters. Some planar radiation detector devices are made of near intrinsic, highly resistive bulk material (in particular diamond, but also CdTe and CdZnTe). In those cases, the electric field profile and the charge transport parameters can be considered to be independent of their position. Full depletion is reached at all bias voltages used (i.e. the capacitance does not change with applied bias), which can simplify the analysis. However, in many diodes, these simplifications are not valid, and the capacitance–voltage (C–V) characterization is the commonly used technique to evaluate the doping profile of a diode. The technique relies on the fact that the depletion width W of a reverse biased space charge region of a semiconductor junction depends on the applied voltage [25]. Assuming a diode with parallel plane electrodes and a one side abrupt p–n junction, the relationship between the donor profile in the n-type region and the depletion width W is given by the following expression:

$$N_D(W) = \frac{2}{q\varepsilon A^2 \dfrac{\mathrm{d}\left(C^{-2}\right)}{\mathrm{d}V}} \tag{3}$$

where C is the capacitance of the junction and W is defined as follows:

$$W = \frac{\varepsilon A}{C} \tag{4}$$

According to Eq. (3), it is very important that the area (A) of the active region of the device is measured precisely for an accurate calculation of the doping profile.

The procedure adopted for the calculation of the doping profile in the n-type region of the device under study, hereafter referred to as DUS1, through Eqs (3, 4), is shown step by step in Fig. 2. It is worth noting that both the electrical measurements and the IBIC measurement were carried out at room temperature.

The doping profile of the bulk is determined by fitting the almost linear curve $1/C^2$–V in Fig. 2. DUS1 is a commercial silicon p–i–n photodiode (Hamamatsu S1223) that is commonly used in ion beam analysis laboratories [1, 17], and its features and method of handling in the measurements are given in Appendix II. Results for a second type of device — an n-type float zone silicon detector, named DUS2 — are also presented in this publication. The features of DUS2, as well as its C–V characterization for estimating its dopant concentration using the proposed procedure, are presented in Appendix III.

An alternative method to evaluate the doping profile is the spreading resistance (SR) technique [25]. Unlike C–V characterization, the SR method is a destructive technique and, therefore, is not generally used. Moreover, the conversion of measured SR data to a doping concentration profile depends very much on the

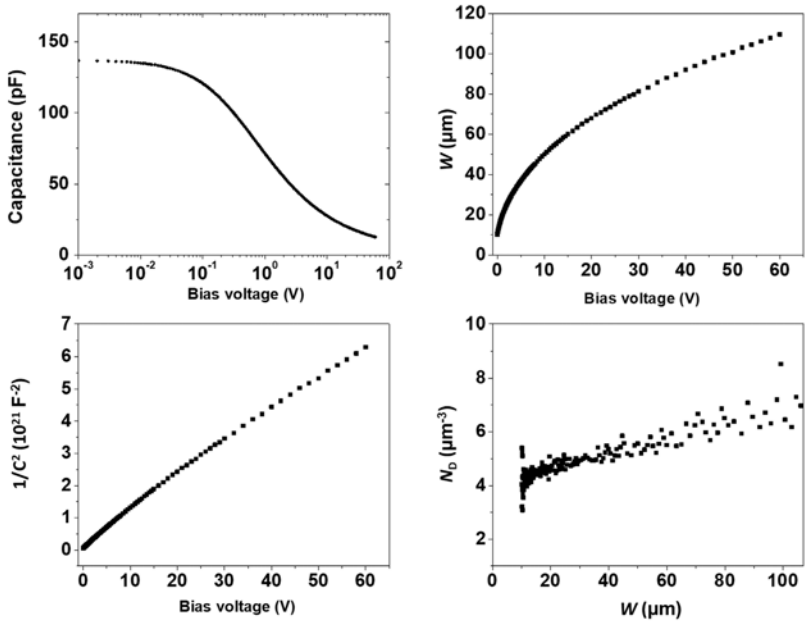

FIG. 2. Top left: capacitance–voltage curve of DUS1. Top right: depletion layer extension versus bias voltage, calculated from Eq. (4). Bottom left: $1/C^2$ versus bias voltage. Bottom right: doping profile calculated from Eq. (3), assuming an electrode area of 13.8 mm^2. The origin of the horizontal axis corresponds to the position of the junction (courtesy of Ž. Pastuović, Australian Nuclear Science and Technology Organisation).

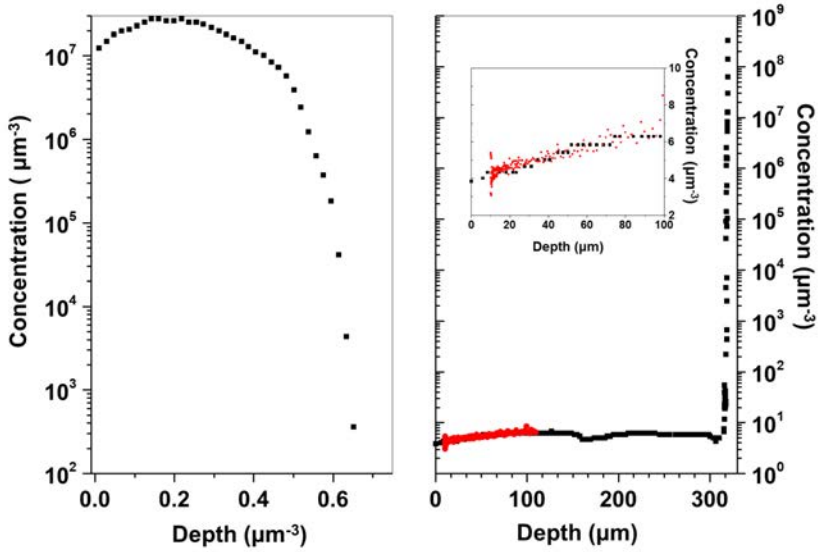

FIG. 3. Acceptor (left) and donor (right) concentration profiles of DUS1 from a spreading resistance measurement (courtesy of G. Vizkelethy, Sandia National Laboratories). The inset (right) shows a comparison between the donor doping profiles evaluated by the spreading resistance (black markers) and capacitatnce–voltage (red markers) techniques, assuming an effective electrode area of 13.8 mm^2.

algorithm. However, the SR method provides profiles of any combination of layers (in this case, of both the p- and n-type regions) with a very high resolution and no depth limitation. SR measurements are commercially available and can be used to verify profiles obtained from *C–V* characterization. Figure 3 shows the doping profiles of the two regions of DUS1 evaluated by the SR technique. The SR profile in the n-type region corresponds to the donor concentration profile, if an effective area of 13.8 mm^2 is assumed.

2.3. ELECTROSTATICS IN ONE DIMENSION UNDER STEADY STATE CONDITIONS

As mentioned in Section 1, the model presented in this publication is based on an accurate knowledge of the device's electrostatics, induced by a constant bias applied to the electrodes. This means that steady state conditions can be considered (Assumption I). For the case of a semiconductor device of thickness *d* with a planar

geometry, the problem can be further simplified by restricting the analysis of the electrostatics to only one dimension (Assumption II). This assumption applies when considering perpendicular irradiation of the front contact electrode and assuming that the trajectories of the high energy ion projectiles (megaelectronvolt energy range) in a material are nearly straight lines [20]. Under these two assumptions, the continuity and Poisson equations become as follows:

$$\begin{cases} \dfrac{\partial}{\partial x}\left(D_{\mathrm{e}} \dfrac{\partial n}{\partial x} - v_{\mathrm{e}} n \right) - R_{\mathrm{e}} + G_{\mathrm{e}} = 0 \\ \dfrac{\partial}{\partial x}\left(D_{\mathrm{h}} \dfrac{\partial p}{\partial x} - v_{\mathrm{h}} p \right) - R_{\mathrm{h}} + G_{\mathrm{h}} = 0 \\ \dfrac{\partial^2 \varphi}{\partial x^2} = -\dfrac{\partial E}{\partial x} = -\dfrac{\rho}{\varepsilon} = -\dfrac{q\left(N_{\mathrm{D}} - N_{\mathrm{A}} + p - n \right)}{\varepsilon} \end{cases} \tag{5}$$

Equation (5) gives the electric field profiles at each point of the device for different bias voltages. The drift velocity profiles $v_{\mathrm{e,h}}$ are determined from the electric field profiles. It is assumed that the terminal at $x = d$ is grounded, the bias voltage V is applied at $x = 0$, (Assumption III) and the contacts are ohmic (Assumption IV). It is further assumed that the device is fully depleted, hence $d = W$. Then, the relevant boundary equations are the following:

$$\begin{cases} \varphi(x=0) = V + V_{\mathrm{bi}} \\ \varphi(x=d) = 0 \end{cases} \tag{6}$$

$$\begin{cases} n(x=0) = n_0(x=0) \\ n(x=d) = n_0(x=d) \end{cases} \tag{7}$$

$$\begin{cases} p(x=0) = p_0(x=0) \\ p(x=d) = p_0(x=d) \end{cases} \tag{8}$$

where n_0 and p_0 are the carrier concentrations in thermal equilibrium conditions.

The built-in potential V_{bi} is given by the following equation:

$$V_{\mathrm{bi}} = \varphi(x=d) - \varphi(x=0) = \frac{k_{\mathrm{B}} T}{q} \ln\left[\frac{p_0(x=0) n_0(x=d)}{n_{\mathrm{i}}^2} \right] \tag{9}$$

where n_{i} is the intrinsic charge carrier concentration, k_{B} is the Boltzmann constant and T is the temperature.

To solve the system Eq. (5), it is convenient to adopt the following functions:

$$\begin{cases} \varphi_{\mathrm{N}} = \dfrac{q}{k_{\mathrm{B}}T}\varphi = \dfrac{\varphi}{\varphi_{\mathrm{th}}} \\ f_{\mathrm{h}} = \varphi_{\mathrm{N}} - \ln\left(\dfrac{p}{n_{\mathrm{i}}}\right) \\ f_{\mathrm{e}} = \varphi_{\mathrm{N}} - \ln\left(\dfrac{n}{n_{\mathrm{i}}}\right) \end{cases} \tag{10}$$

with $\varphi_{\mathrm{th}} = k_{\mathrm{B}}T/q$.

The relevant continuity and Poisson equations can then be written as follows:

$$\begin{cases} -n_{\mathrm{i}}\varphi_{\mathrm{th}}\dfrac{\partial}{\partial x}\left(\mu_{\mathrm{e}}e^{\varphi_{\mathrm{N}}-f_{\mathrm{e}}}\dfrac{\partial f_{\mathrm{e}}}{\partial x}\right) - R_{\mathrm{e}} = 0 \\ n_{\mathrm{i}}\varphi_{\mathrm{th}}\dfrac{\partial}{\partial x}\left(\mu_{\mathrm{h}}e^{-\varphi_{\mathrm{N}}+f_{\mathrm{h}}}\dfrac{\partial f_{\mathrm{h}}}{\partial x}\right) - R_{\mathrm{h}} = 0 \end{cases} \tag{11}$$

$$\frac{\partial^2\varphi}{\partial x^2} = -\frac{q}{V_{\mathrm{th}}\varepsilon}\left[N_{\mathrm{D}} - N_{\mathrm{A}} + n_{\mathrm{i}}\left(e^{-\varphi_{\mathrm{N}}+f_{\mathrm{h}}} - e^{\varphi_{\mathrm{N}}-f_{\mathrm{e}}}\right)\right] \tag{12}$$

with the following boundary conditions:

$$\begin{cases} f_{\mathrm{e,h}}(x=0) = \dfrac{\varphi}{\varphi_{\mathrm{th}}} \\ f_{\mathrm{e,h}}(x=d) = 0 \end{cases} \tag{13}$$

$$\begin{cases} \varphi_{\mathrm{N}}(x=0) = \dfrac{\varphi}{\varphi_{\mathrm{th}}} - \ln\left[\dfrac{p(x=0)}{n_{\mathrm{i}}}\right] \\ \varphi_{\mathrm{N}}(x=d) = \ln\left[\dfrac{n(x=d)}{n_{\mathrm{i}}}\right] \end{cases} \tag{14}$$

Figure 4 shows the electrostatic potential and the electric field profiles of DUS1 at different bias voltages. The carrier drift velocity profiles, $\boldsymbol{v}_{\mathrm{e,h}} = \mu_{\mathrm{e,h}}\boldsymbol{E}$, shown in Fig. 5, were obtained using an expression widely used for calculating carrier mobility in silicon, which incorporates the ionized impurity concentration [26, 27]; see Appendix IV for details.

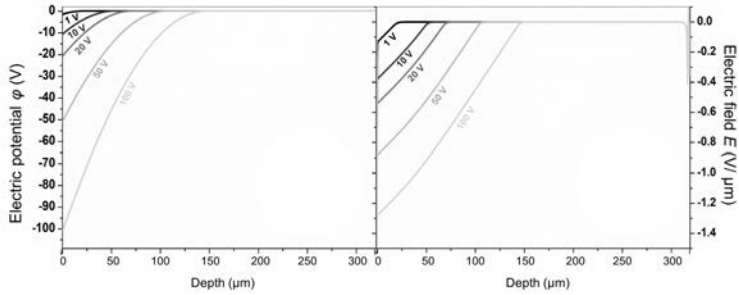

FIG. 4. Electrical features of DUS1. Left: electrostatic potential. Right: electric field profile.

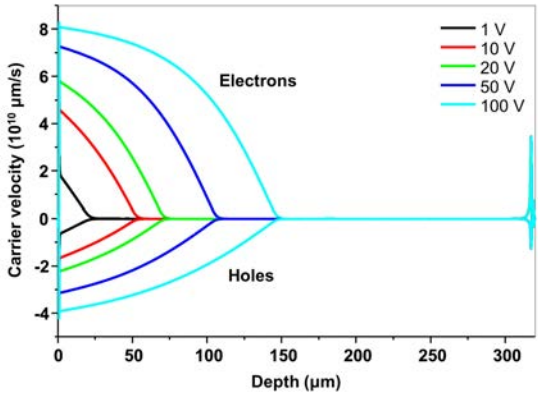

FIG. 5. Electron and hole drift velocity profiles at different bias voltages for DUS1.

2.4. QUASI-STEADY-STATE CONDITIONS

In most applications, semiconductor devices operate in a quasi-steady-state mode in which the excess charge produced by radiation interactions does not significantly perturb the electric field within the detector (Assumption V). Consequently, the continuity equations can be decoupled from the Poisson equation. These assumptions are routinely employed in the analysis of semiconductor detectors [28–30] and also used here as stated. Further, the electron and hole

continuity equations can be decoupled and the generation–recombination terms can be linearized (Assumption VI). The linearization of the recombination term is expressed as follows:

$$\begin{cases} R_{\mathrm{e}} = \dfrac{n}{\tau_{\mathrm{e}}} \\ R_{\mathrm{h}} = \dfrac{p}{\tau_{\mathrm{h}}} \end{cases} \tag{15}$$

This approximation is valid when (i) the excess carrier concentration is small compared to the number of available trapping and recombination centres and (ii) the de-trapping time is small compared to the transit time. In this case, the rate of removal of carriers is proportional to the carrier concentration. Assumption V and Assumption VI lead to the following spatial–temporal equation for the concentration of excess carriers within the semiconductor:

$$\begin{cases} \dfrac{\partial n^*}{\partial t} = \dfrac{\mathrm{d}}{\mathrm{d}x}\left(D_{\mathrm{e}} \dfrac{\mathrm{d}}{\mathrm{d}x} n^* - v_{\mathrm{e}} n^* \right) - \dfrac{n^*}{\tau_{\mathrm{e}}} + G_{\mathrm{e}} \\ \dfrac{\partial p^*}{\partial t} = \dfrac{\mathrm{d}}{\mathrm{d}x}\left(D_{\mathrm{h}} \dfrac{\mathrm{d}}{\mathrm{d}x} p^* - v_{\mathrm{h}} p^* \right) - \dfrac{p^*}{\tau_{\mathrm{h}}} + G_{\mathrm{h}} \end{cases} \tag{16}$$

where n^* and p^* represent the excess electron and hole concentrations, respectively.

The initial condition for the problem is the following:

$$n^*\left(x, t = 0\right) = 0 \tag{17}$$

where $x \in [0, d]$ is the integration domain (i.e. the set of points within the semiconductor).

For the mapping of charge pulses, the generation term is selected to be an impulse of the unit charge at x_0 (i.e. $G_{\mathrm{e}} = G_{\mathrm{h}} = G = \delta(x - x_0)\delta(t)$), where δ is the Dirac delta function.

The parameters of the excess carrier equation, including the mobility, vary with position and electric field. Similarly, the free carrier lifetime in silicon is also space dependent and often described using empirical expressions. In this work, the formulation of Ref. [27] was adopted (see Appendix IV).

2.5. MODELLING OF THE INDUCED CHARGE

The current induced in the electrodes by the motion of charge carriers can be estimated using the weighting potential method and the formulation proposed in Ref. [31], which is an extension of the well known Shockley–Ramo theorem [32, 33]. Using this method, the charge induced on an individual electrode connected to a common circuit can be determined [34]. Here, the analysis is confined to cases in which the electrode potential is not influenced by charge motion, which is consistent with the assumptions used to decouple the semiconductor equations.

The total charge Q induced at the sensing electrode at time t is the sum of the charges Q_e and Q_h generated at a certain position x_0 by the motion of electrons and holes, and is given by the following expression:

$$Q(t) = Q_e(t) + Q_h(t) = -q\int_0^t dt' \int_0^d dx \left(n^* v_e + p^* v_h \right) \frac{\partial E}{\partial V} \tag{18}$$

The spatial–temporal evolution of n^* and p^* can be calculated by solving the electron (hole) continuity equations with initial conditions $n(x, t = 0) = p(x, t = 0) = \delta(x - x_0)$. Details on the theory leading to Eq. (18) are given in numerous publications (e.g. Refs [20, 35, 36]). It is important to understand that the decoupling of the electron and hole contributions in Eq. (18) implies not only the negligible interaction of electrons and holes, but also the linear superposition of the electron–hole recombination and trapping processes.

The term $E^+ = \partial E / \partial V$ is the Gunn weighting field, defined as the partial derivative of the applied electric field $\boldsymbol{E}$ with respect to the bias voltage V applied to the sensing electrode while the voltage is kept constant on all the other electrodes. The Gunn weighting potential, $\varphi^+ = \partial \varphi / \partial V$, is similarly defined. The calculation of these terms can be effectively carried out by solving the following differential equations, which are extracted from the continuity and Poisson equations (i.e. Eqs (11, 12)):

$$\begin{cases} \dfrac{\partial}{\partial x}\left[\mu_e n \left(\dfrac{\varphi^+}{\varphi_{th}} \dfrac{\partial f_e}{\partial x} - f_e^+ \dfrac{\partial f_e}{\partial x} + \dfrac{\partial f_e^+}{\partial x} \right) \right] = 0 \\ \dfrac{\partial}{\partial x}\left[\mu_h p \left(-\dfrac{\varphi^+}{\varphi_{th}} \dfrac{\partial f_h}{\partial x} + f_h^+ \dfrac{\partial f_h}{\partial x} + \dfrac{\partial f_h^+}{\partial x} \right) \right] = 0 \end{cases} \tag{19}$$

$$\frac{\partial^2 \varphi^+}{\partial x^2} = -\frac{q}{\varepsilon}\left[p\left(f_{\mathrm{h}}^+ - \frac{\varphi^+}{\varphi_{\mathrm{th}}} \right) + n\left(f_{\mathrm{e}}^+ - \frac{\varphi^+}{\varphi_{\mathrm{th}}} \right) \right] \tag{20}$$

with the following assumptions:

$$\frac{\partial \mu_{\mathrm{e,h}}}{\partial V} = 0 \text{ and } \frac{\partial R}{\partial V} = 0 \tag{21}$$

The boundary conditions are easily derived from Eqs (13, 14).

$$\begin{cases} f_{\mathrm{e,h}}^+ (x = 0) = \dfrac{1}{\varphi_{\mathrm{th}}} \\ f_{\mathrm{e,h}}^+ (x = d) = 0 \end{cases} \tag{22}$$

$$\begin{cases} \varphi^+ (x = 0) = 1 \\ \varphi^+ (x = d) = 0 \end{cases} \tag{23}$$

The profiles of the Gunn weighting potential, $\varphi^+ = \partial\varphi/\partial V$, and the Gunn weighting field, $E^+ = \partial E/\partial V$, for DUS1 at different bias voltages are shown in Fig. 6. Also plotted in the same figure are the electric field and potential shown in Fig. 4 for comparison with the Gunn equivalent parameter.

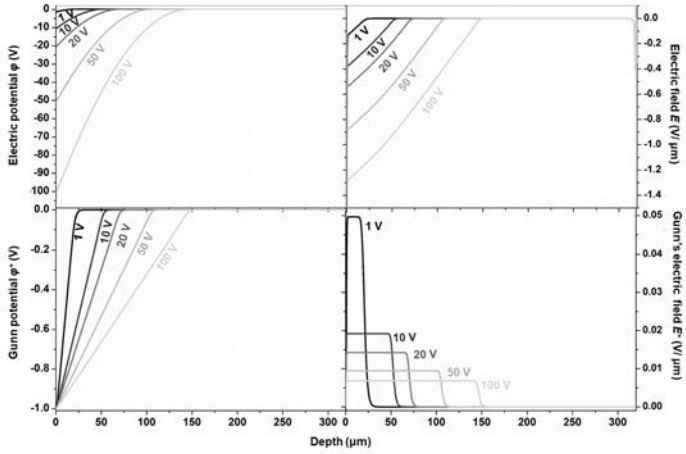

FIG. 6. Electrical profiles of DUS1. Top left: electrostatic potential; top right: electric field; bottom left: Gunn potential; bottom right: Gunn electric field.

It is also worth noting that the capacitance of the diode using Gauss's law and the Gunn weighting field can be easily evaluated as follows:

$$\begin{cases} \boldsymbol{E}^{+} = \dfrac{\partial \boldsymbol{E}}{\partial V} \\ \nabla \cdot \boldsymbol{E} = \dfrac{\rho}{\varepsilon} \end{cases} \Rightarrow \nabla \cdot \boldsymbol{E}^{+} = \frac{1}{\varepsilon}\frac{\partial \rho}{\partial V} \tag{24}$$

if complete depletion is assumed.

With Assumption II, the following equation is obtained:

$$E^{+}(W) - E^{+}(0) = \frac{1}{\varepsilon}\frac{\partial}{\partial V}\int_{0}^{W} \rho \mathrm{d}x = \frac{1}{\varepsilon}\frac{\partial q_{\mathrm{T}}}{\partial V} = \frac{1}{\varepsilon}c \tag{25}$$

where q_{T} is the total space charge within the depletion region W (which is a function of the applied bias voltage, V) and c is the capacitance per unit area.

Therefore, the measured capacitance (C) is related to the Gunn weighting field by the following expression:

$$C(V) = \varepsilon A\left\{\left[E^{+}(W(V)) - E^{+}(0)\right]\right\} \tag{26}$$

where A is the area of the electrodes.

Figure 7 shows a comparison of the experimental C–V characteristics of DUS1 with the curve calculated using Eq. (26). Figure 7 shows excellent agreement of the experimental data with the simulated data obtained by solving Eqs (11, 12) and Eqs (19, 20) and using the doping profile extracted from SR profiling. The area A of the electrode was set to 13.8 mm^2.

The total charge Q — and therefore the CCE, defined as Q/Q_0 — can be modelled using two approaches: (i) by numerically solving the adjoint equations of semiconductors as described in Section 2.6 and (ii) by using a semianalytical expression, which can be easily applied without the use of any finite element method code.

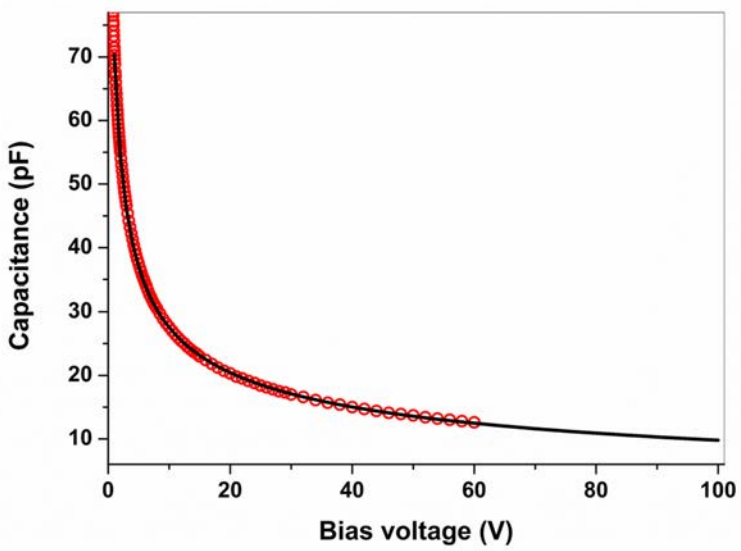

FIG. 7. Capacitance–voltage characteristics of DUS1. Red markers: experimental data; solid line: capacitance calculated with Eq. (26).

2.6. THE ADJOINT EQUATION METHOD FOR DETERMINING THE INDUCED CHARGE

When it comes to modelling radiation induced effects, the time dependent non-linear carrier concentration equations need to be solved for each point within the detector. An efficient method to evaluate the induced charge is based on the solution of the adjoint continuity equation, which can be constructed from Eq. (18), since it involves only linear operators (see Refs [20, 29, 30] and references therein).

If the free carrier generation terms are defined in the following manner:

$$\begin{cases} G_{\mathrm{e}}^{+} = -v_{\mathrm{e}} \cdot \boldsymbol{E}^{+} - \nabla \cdot \left(D_{\mathrm{e}} \boldsymbol{E}^{+} \right) \\ G_{\mathrm{h}}^{+} = v_{\mathrm{h}} \cdot \boldsymbol{E}^{+} + \nabla \cdot \left(D_{\mathrm{h}} \boldsymbol{E}^{+} \right) \end{cases} \tag{27}$$

then Eq. (26) corresponds to the Green function of the continuity equations for the two carrier types.

As a result, it is possible to calculate the electron and hole contributions to the induced signal charge by solving the continuity equations, expressed using the adjoint form described in Ref. [37], as follows:

$$\begin{cases} \dfrac{\partial n^+}{\partial t} = \nabla \cdot \left(D_{\mathrm{e}} \nabla n^+ \right) + \boldsymbol{v}_{\mathrm{e}} \cdot \nabla n^+ - \dfrac{n^+}{\tau_{\mathrm{e}}} + G_{\mathrm{e}}^+ \\ \dfrac{\partial p^+}{\partial t} = \nabla \cdot \left[D_{\mathrm{h}} \nabla p^+ \right] + \boldsymbol{v}_{\mathrm{h}} \cdot \nabla p^+ - \dfrac{p^+}{\tau_{\mathrm{h}}} + G_{\mathrm{h}}^+ \end{cases} \tag{28}$$

Within Assumption II, these equations become the following:

$$\begin{cases} \dfrac{\partial n^+}{\partial t} = \dfrac{\mathrm{d}}{\mathrm{d}x}\left(D_{\mathrm{e}} \dfrac{\mathrm{d}n^+}{\mathrm{d}x} \right) + v_{\mathrm{e}} \dfrac{\mathrm{d}n^+}{\mathrm{d}x} - \dfrac{n^+}{\tau_{\mathrm{e}}} + G_{\mathrm{e}}^+ \\ \dfrac{\partial p^+}{\partial t} = \dfrac{\mathrm{d}}{\mathrm{d}x}\left(D_{\mathrm{h}} \dfrac{\mathrm{d}p^+}{\mathrm{d}x} \right) + v_{\mathrm{h}} \dfrac{\mathrm{d}p^+}{\mathrm{d}x} - \dfrac{p^+}{\tau_{\mathrm{h}}} + G_{\mathrm{h}}^+ \end{cases} \tag{29}$$

The solution of these adjoint equations yields spatial and temporal maps of the charge induced at the sensing electrode as a consequence of the motion of free electrons and holes generated in $x \in [0, d]$, as follows:

$$Q(x,t) = Q_{\mathrm{e}}(x,t) + Q_{\mathrm{h}}(x,t) = q\left[n^+(x,t) + p^+(x,t) \right] \tag{30}$$

In many applications, the physical observable is the total induced charge. Therefore, Eq. (30) can be considered further in steady state conditions, expressed as follows:

$$\begin{cases} \dfrac{\mathrm{d}}{\mathrm{d}x}\left(D_{\mathrm{e}} \dfrac{\mathrm{d}n^+}{\mathrm{d}x} \right) + v_{\mathrm{e}} \dfrac{\mathrm{d}n^+}{\mathrm{d}x} - \dfrac{n^+}{\tau_{\mathrm{e}}} + G_{\mathrm{e}}^+ = 0 \\ \dfrac{\mathrm{d}}{\mathrm{d}x}\left(D_{\mathrm{h}} \dfrac{\mathrm{d}p^+}{\mathrm{d}x} \right) + v_{\mathrm{h}} \dfrac{\mathrm{d}p^+}{\mathrm{d}x} - \dfrac{p^+}{\tau_{\mathrm{h}}} + G_{\mathrm{h}}^+ = 0 \end{cases} \tag{31}$$

with the following homogeneous boundary conditions:

$$\begin{cases} n^+(x=0) = n^+(x=d) = 0 \\ p^+(x=0) = p^+(x=d) = 0 \end{cases} \tag{32}$$

used to obtain the electron and hole contributions to the total induced charge profiles. Figure 8 shows the electron and hole contributions to the induced charge, as evaluated by solving Eq. (31) for DUS1 with an applied reverse bias voltage of 50 V. The electrostatic transport and Gunn field profiles are as depicted in Figs 4–6 and the carrier lifetimes are given by Eq. (15); the numerical parameters used in the mobility and lifetime models are reported in Appendix IV.

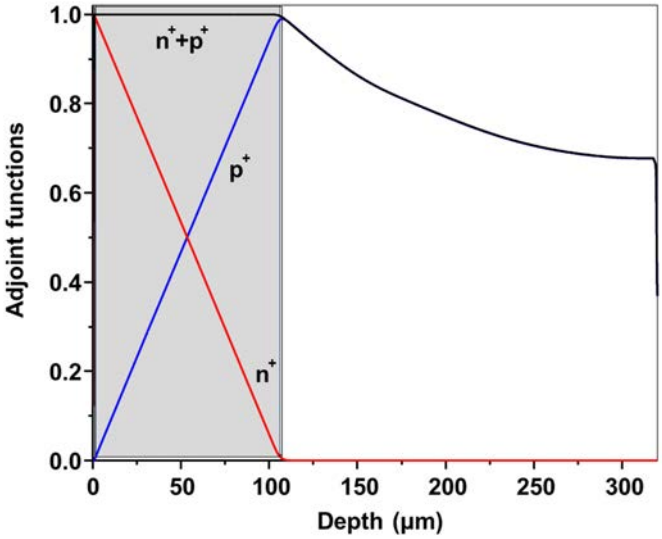

FIG. 8. Electron (n^+) and hole (p^+) adjoint concentrations of DUS1 for an applied bias voltage of 50 V. The shaded region indicates the depletion layer.

Because the lifetime of free carriers far exceeds their drift time, almost all the free carriers generated inside the depletion region are collected. This explains the fact that the plateaux extends throughout the depletion region and coincides with the region that has a non-zero Gunn weighting potential. Outside the depletion region (i.e. in the neutral region where no electric field occurs), the n^+ profile is null because hardly any electrons (the majority carriers) enter the depletion region owing to the opposite electric field. On the other hand, the hole contribution follows a typical exponential profile, which is due to hole injection into the depletion region by diffusion, resulting in an induced signal described by Eq. (30) [20].

In summary, starting with elementary electrostatics, a formalism has been developed for determining the induced charge generated by an elementary charge moving within the semiconductor. The adjoint equation method is a time saving and powerful procedure that can be used to calculate the charge induced at the sensing electrode by the motion of free charges generated inside a semiconductor device. It is not limited by the geometry of the device; however, more complex structures may require numerical approaches to establish the necessary parameters. Some examples of existing software that can be used for this purpose are included in Appendix V. The complete formalism of the CCE data analysis, including the effects of ion–matter interaction, will be elaborated in Sections 3 and 5.

3. ENERGETIC ION–MATTER INTERACTIONS

3.1. INTERACTION MECHANISMS

There are two dominant interaction mechanisms responsible for energy loss of an energetic ion as it travels through matter within the energy range that are relevant for this publication. These are: (a) Coulomb interactions of the charged ions with the electrons in the material [38] and (b) elastic collisions between the ion and the atoms in the material (leading to Rutherford backscattering, for example [39]). These are conventionally referred to as electronic and nuclear energy loss, respectively.

3.1.1. Electronic energy loss and charge carrier generation

Electronic energy loss is the dominant interaction mechanism at high (megaelectronvolt range and above) ion energies. During each electronic interaction, the ion can lose only a small fraction of its overall energy[2] and, hence, many interactions will take place until the ion has lost sufficient energy for nuclear stopping to become significant. The energy transferred to the electron either results in its excitation to a higher energy level within the band structure of the atom, molecule or solid, or it can be sufficient to eject the electron from its atom, thus leading to ionization. The resultant electron can also have sufficient energy to cause further excitations and ionizations through Coulomb interactions with the surrounding matter; such energetic electrons are sometimes called delta rays. Their range is normally short (compared to the ion range)[3] and the ionization volume can be considered as a cylinder with a diameter of a few nanometres around the incident ion track [9].

The above processes are responsible for the generation of free charge carriers within a semiconductor material under ion irradiation. Thus, free charge carriers are expected to be created all along the ion track until the electronic stopping contribution to the ion energy loss can be considered negligible.

---

[2] An ion has a much higher mass than an electron, and the energy transferred in a collision between an ion and an electron, E_{trans}, is limited by the momentum conservation condition, so that $E_{trans} \leq 4(m_e/m_{ion})E_{ion}$, where m_{ion} and m_e are the mass of the ion and the electron, respectively, and Eion is the energy of the ion before the collision.

[3] Highly energetic electrons can also be the product of interactions of other types of ionizing radiation — i.e. high energy charged particle beams (e.g. electrons, muons), X rays and γ rays — with matter. Hence, the effects of these types of radiation on matter are very similar to the processes induced by the electronic stopping of ion beams.

3.1.2. Nuclear energy loss and radiation damage

Nuclear energy loss dominates at low ion energies (below 100 keV) for heavy ions and is hence most significant towards the end of the ions' track into the target. Similarly to electronic stopping, many elastic atomic collisions will usually take place before the initial ion has lost all its energy and comes to rest (neglecting its thermal energy and, hence, velocity). The energy and momentum transfer between the ion and the target atoms can lead to the displacement of the target ion from its initial position if the energy transferred is larger than the displacement energy, which needs to be exceeded in order for the atom to leave its position. In crystalline solids, this will produce an interstitial vacancy complex, referred to as a Frenkel pair [40]. Thermal energies may be sufficient for the vacancy interstitial pair to recombine, or for individual point defects to migrate and combine with other pre-existing defects to form more complex defect structures within the material. These processes are often not well understood, even in well controlled and established materials such as silicon [41]. These defects cause additional electronic states to be created within the band structure of the material, which can act as charge carrier traps and, hence, modify the free charge carrier drift lifetimes. Additionally, if the number of defects introduced is sufficiently large, they may also influence additional electronic properties, including scattering mechanisms for charge transport, which can influence the charge carrier drift mobility as well as the effective doping profile. Ion beam induced radiation damage and its associated effects on the electronic properties are concentrated at the end of the ion track, where nuclear stopping contributes the most.

Hence, it is expected that radiation damage relates to the energy deposited by the ion beam through processes associated with nuclear stopping. This is reflected in the concept that the damage introduced by different particle species and energies can be quantitatively compared if the non-ionizing energy loss (NIEL) for each scenario [4–6] can be estimated. For more details on the NIEL calculations and their underlying assumptions, see Ref. [42].

3.2. ION BEAM TRACK PARAMETERS

The exact details of each individual scattering event of an ion along its track are impossible to predict accurately, and thus the energy loss, energy deposition, ion positions and vacancies created by an ion beam in a target are quoted as the average values for many ions. This leads to the use of the characteristic parameters of the linear stopping power, the ion beam range and its energy straggling, which are discussed in detail in Sections 3.2.1–3.2.3. These parameters are determined

from the mass and energy (and hence velocity) of the ion. The charge state of the incident ion beam on a thick solid target rarely plays a significant role, as the ions will pick up or lose electrons as they travel through matter, depending on their velocity. Therefore, if the same isotope beam with a different charge state but the same energy (i.e. velocity) is used, the charge state of the ions within the target will become the same for all ions after the beam has travelled through the initial sections of the target. At the end of its track, the ion will pick up electrons from the target and neutralize [38].

In the following sections, it is assumed that a monoenergetic ion beam with initially negligible beam diameter in the y–z plane of a standard Cartesian coordinate system is perpendicularly incident onto a target at the ($y = 0$, $z = 0$) position.

3.2.1. Linear stopping power

In this case, the energy loss per ion per distance travelled into the target (x direction) is known as the linear stopping power $-\mathrm{d}E/\mathrm{d}x$, which has an electronic and a nuclear stopping component and is often written as follows [43]:

$$-\frac{\mathrm{d}E}{\mathrm{d}x} = \left(-\frac{\mathrm{d}E}{\mathrm{d}x}\right)_{\text{electronic}} + \left(-\frac{\mathrm{d}E}{\mathrm{d}x}\right)_{\text{nuclear}} \tag{33}$$

3.2.2. Straggling

Owing to the probabilistic nature of the processes described, the energy distribution of the beam will broaden as the beam travels through a material, as some ions may lose slightly more energy than others while travelling the same distance in the x direction. The width of the energy distribution will increase, which is described as ‘energy straggling’. In parallel, ions will also be scattered away from the origin of the y–z plane along the x axis, although their average position will remain in line with the initial beam direction (i.e. along the x axis). The broadening of the distribution of ions within the y–z plane is referred to as ‘lateral straggling’, whereas the spread of ions along the x axis is called ‘longitudinal straggling’ [38].

3.2.3. Ion range

The ion range for a particular beam energy and ion species is defined as the depth along the x axis where half of the ions have stopped within the material. If

the linear energy loss and straggling values (as a function of energy) are known, then these can be used to evaluate the ion range [38].

3.3. CALCULATION OF CARRIER AND DAMAGE GENERATION PROFILES USING MONTE CARLO SIMULATIONS

As discussed in Section 3, the charge carrier generation profile within a semiconductor as a function of depth can be approximated by the electronic energy deposition by the incident ion beam into the target, whereas the damage profile can be approximated using the nuclear stopping power related to the NIEL.

Monte Carlo simulations are used to evaluate both these aspects of the interaction of ions with matter. These simulations often use the binary collision approximation to provide a representative sample of ion trajectories that allows the prediction of the energy deposition, ion implantation and displacement, as well as the resulting vacancy and interstitial profiles. Commonly used Monte Carlo simulation software used for the energy and ion species of interest to this work are SRIM [10] and MARLOWE [44, 45]. For more details on these codes, see Refs [16, 46]. The work presented in this publication is limited to ion irradiations, and SRIM was adopted as one of the main tools, as it is freely accessible for non-commercial purposes and easy to use. It is possible that the concepts used in this work can be expanded to a broader range of codes and radiation types (e.g. photons, neutrons, high energy electrons), but this is beyond the scope of this publication.

SRIM allows the user to specify the ion species (energy and isotope) and incidence angle of the incident beam, as well as the composition of the target, which can be made up of multiple and composite layers; default values are provided for a wide range of material constants (e.g. density, average mass number of the element, binding energy, displacement energy, surface binding energy) [16]. Note that the simulation assumes that the target is amorphous; the effects of lattice geometry — in particular channelling — are not taken into account. Hence, if channelling occurs during the damaging or probing ion beam (PIB) irradiations, then the experimental data may deviate significantly from the simulated values.

The two key SRIM outputs used in this work are the following:

— The ionization distribution, which reflects the charge carrier generation profile of the PIB. SRIM does not simulate the charge transport of the created charge carriers, and hence the ionization profile does not include any charge spread or loss due to diffusion. The damage induced by the PIB is considered negligible in this work, which is a reasonable approximation, as the PIB fluences are low compared to the DIB fluences.

— The generated vacancy distribution, which reflects the damage profile created by the DIB. It is important to note that SRIM does not take into account any vacancy mobility, diffusion, combination or recombination effects. Hence, the vacancy profile calculated by SRIM can be considered as the 'generated' vacancy distribution that is expected if each vacancy produced is completely immobile. The physical vacancy distribution in a material held at room temperature during and after the irradiation may be very different from the SRIM simulated one. However, for the purposes of this work, it is not necessary to know the absolute physical room temperature vacancy distribution resulting from the ion irradiation. The assumption made is that the SRIM simulated vacancy profile is proportional to the amount of damage produced in the irradiated material. Hence, the simulated vacancy profiles act as a means to normalize between the damage produced by different ion species and energies, similar to the NIEL concept or the concentration of primary defects explored in Ref. [6] as a means to quantify radiation hardness in semiconductors.

Examples of nuclear and electronic stopping power profiles and the associated SRIM simulated vacancy profile are shown in Fig. 9, which illustrates the close overlap between the nuclear stopping power of the damaging beam and the vacancy distribution. The ion stopping power versus depth (and its associated damage profile) is often referred to as a Bragg curve and its increase towards the end of the ion range as the Bragg peak.

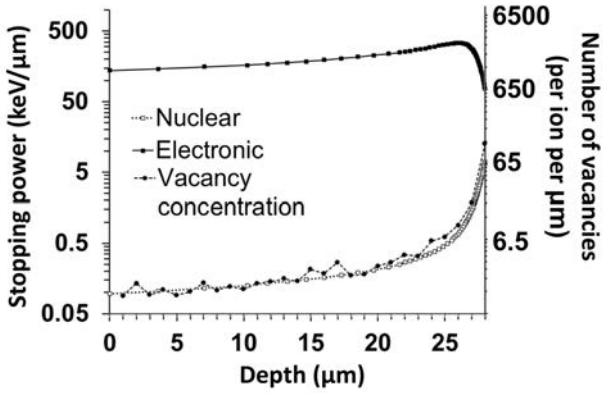

FIG. 9. SRIM simulated nuclear and electronic stopping powers and vacancy profile for 5485.6 keV α particles incident on silicon, obtained using a displacement energy of 21 eV, a lattice binding energy of 1.5 eV and a surface binding energy of 3 eV.

4. EXPERIMENTAL PROCEDURES

4.1. DESIGN OF EXPERIMENTAL PROCEDURES

The design of the experimental procedure presented here is based on the use of (i) accelerated ions to induce damage in selectively irradiated regions of a device by displacing lattice atoms in collision cascades and (ii) ions with the same or different range to probe the induced damage. In principle, it is possible to carry out equivalent studies by adapting these experimental procedures using radioisotope and broad beam irradiations of multiple diodes (potentially combined with a well designed selection of absorbers to modify the incident ion energy in different regions). However, it is crucial to ascertain that the dopant profiles of the diodes are initially the same and their CCEs are comparable. In addition, small area irradiations as presented in this work have the advantage that the induced damage causes negligible changes to the overall leakage current and, hence, negligible noise levels in the subsequent CCE measurements. In broad beam irradiation studies, the increased leakage current generated by the higher damaging beam fluence can significantly compromise the experimental campaign. For these reasons, microbeam facilities are ideal for the purposes of this work.

The system needs to be simplified so as to be described by a one dimensional model that is consistent with the assumptions presented in Sections 2.3–2.6. Using a highly focused ion microbeam to introduce the damage, deviations from normal incidence of the ions are typically <1° and negligible. The ion trajectories within the material and the volume in which the vacancies are produced by knock-on collisions will usually not follow a perfectly straight line, but the effect can be described in a linear fashion when averaged over many ions. It should be also noted that for the typical beam spot dimensions of micrometre scale, an incident ion rate of a few kilohertz and a typical dwell time of several hundred microseconds per pixel, usually only one ion will be deposited in each pixel per unit dwell time. This may be important, as it means that each cascade formation caused by an incident ion will be completed before any additional cascades occur within the same area [20]. For more details on the estimated timescales of the dynamic processes initiated by an incident ion, see Ref. [47].

The experimental procedures include the following three steps:

(a) Measurement of the CCE in regions of the pristine diode to assess the uniformity of the areas to be irradiated;

(b) Irradiation of N (typically $N = 9$) regions at different fluences with DIBs (preferably at zero, or as low as possible, bias, which is sufficient for DIB particle discrimination and detection; see Section 4.3.3);
(c) Measurement of the CCE in regions irradiated by a range of PIBs at different bias conditions.

Sections 4.2 and 4.3 introduce the associated experimental set-ups and Section 4.3.4 provides details on the selection of the irradiation and measurement parameters used in steps (a) to (c).

4.2. ELECTRONICS AND CALIBRATION

This section describes the electronics used to measure the pulse height and their calibration. The experiment was carried out on diode DUS1, detailed in Appendix II.

4.2.1. Pulse height measurement set-up

To experimentally determine the CCE, the charge induced by the movement of the electron–hole pairs created in the diode by the incident radiation needs to be measured. The signal produced by the induced charge is the same signal that is processed in standard nuclear radiation spectroscopy (e.g. α, β, γ spectroscopy and other ion beam analysis techniques such as Rutherford backscattering, nuclear reaction analysis, particle induced X ray emission); hence, the same electronic chain or chains can be used in CCE measurements. This is illustrated in Fig. 10, which shows a scheme of the experimental set-up: probing ions hit the frontal electrode and generate electron–hole pairs by ionization; the drift of those pairs induces an electric current, which is integrated by the charge sensitive preamplifier. The scheme represents a p–n junction, where the cathode is located at $x = 0$ and the anode, located at $x = d$, is grounded.

Each pulse is fed to a low noise charge sensitive preamplifier, which integrates the induced charge on a feedback capacitor. Details on the principles of operation of the charge sensitive preamplifier can be found in many textbooks (e.g. Refs [38, 48]) and instruction manuals from suppliers [49, 50]. An ideal solution for the coupling of the preamplifier to the sample was adopted at the LIPSION laboratory in Leipzig, Germany [51, 52]: a charge sensitive preamplifier [53] is integrated into the sample holder and directly connected to the device under test. The electronic board is embedded in a metal box and shielded against electromagnetic radiation. Coaxial cables are commonly used to couple the detector to the preamplifier. Since the electronic noise increases with the input

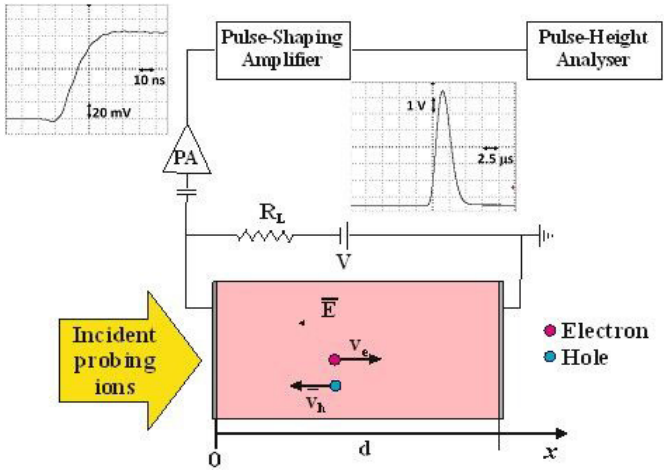

FIG. 10. Schematic of the experimental set-up with an AC coupled arrangement. The bias voltage V *is supplied through a load resistor* R_L*. The oscilloscope traces in the insets illustrate the output signal shapes of a charge sensitive preamplifier (left) and a shaping amplifier (right).*

capacitance, leads between the device under test and the preamplifier need to be as short as possible. The sample needs to be isolated from earth loops, circulating currents and radio frequency pick-up from other electronic components of the experimental set-up [54]. The small output pulses from the preamplifier are then fed into a shaping amplifier. For the selection of shaping time, the following need to be taken into consideration: (i) the time that it takes for the charge carriers to induce the signal, as the shaping time needs to be sufficiently long to process the complete signal, and (ii) the fact that the shaping time also impacts the parallel and series electronic noise contributions to the signal, which depend on the detector and the electric connections [55]. In this work, shaping times of the order of 0.5 µs or 1 µs were used for the best signal to noise ratio. Finally, the pulses from the shaping amplifier are fed into the data acquisition system, usually a multichannel analyser, which stores the amplitude of every event detected from the sample. In the case of IBIC, this signal needs to be stored alongside its associated spatial coordinate. This is usually carried out by generating 'event by event' (or 'list mode' or 'list') files [54]. This has the advantage that event by event off-line analysis can be carried out to investigate signal stability throughout the data acquisition period.

4.2.2. Calibration of the pulse height measurement set-up in terms of CCE

A typical charge pulse height spectrum measured for detection of monoenergetic ions (within the energy resolution limits of the accelerating system) using an IBIC experimental set-up [20] is shown in Fig. 11. The peak position is usually evaluated through a Gaussian fit of the experimental data. The low energy shoulder on the peak can be caused by either incomplete energy deposition or incomplete charge collection, whereas a high energy shoulder may be visible at high event rates owing to pile up. More elaborate algorithms than a simple Gaussian can be used to fit the full shape of the peak (e.g. Ref. [56]), but they do not provide any significant improvement on the model.

To calibrate the electronic chain in terms of the CCE, the signal amplitude (expressed in channel numbers) that corresponds to the amount of free charges Q_0 generated by the energy deposited by the incident radiation pulse or particle (typically ions, X ray or γ photons, or β particles, with ideally monoenergetic or well separated energy values) needs to be known. In most cases, the particle energy is known and hence the charge generated can be calculated using the average number of free charge carriers generated per unit of absorbed energy, ε_{ehp}, which is an intrinsic property of the material; see, for example, Ref. [57]. Then, the equivalent amount of charge can be injected into the electronic chain at the test input capacitor of the preamplifier using a pulse generator [58]. Multiple equivalent energy values can be used to confirm the linearity between the charge signal and its corresponding channel number (see Fig. 12).

However, for practical purposes, if the device under study initially reaches 100% CCE at a sufficiently high applied bias (i.e. full depletion, in order to generate all charges within the active volume, and full charge collection), then the CCE calibration is often carried out by plotting the peak position as a function of the applied bias voltage, as shown in Fig. 13. In this case, the saturation of the signals indicates that the carrier generation occurs entirely within the depletion region and that full charge collection has been reached. The conclusion that saturation of the induced charge with increasing applied bias voltage indicates complete charge collection can be drawn only if the electric field strengths are sufficiently low so that the charge velocity does not reach saturation values. This method has the advantage that constant energy losses (for example, in the metal contact layer) or an accurate knowledge of ε_{ehp} are not needed. The energy loss in the metal contact layer can also be determined using angle resolved measurements, as detailed in Section 4.2.4.

In the example of signal saturation, and hence 100% CCE, shown in Fig. 13, the slope of the linear fit of the peak position as a function of the ion energy is 4.80 ± 0.07 keV per channel. The charge sensitivity is 1330 ± 20 electrons per channel, as evaluated assuming a total collection efficiency (100%)

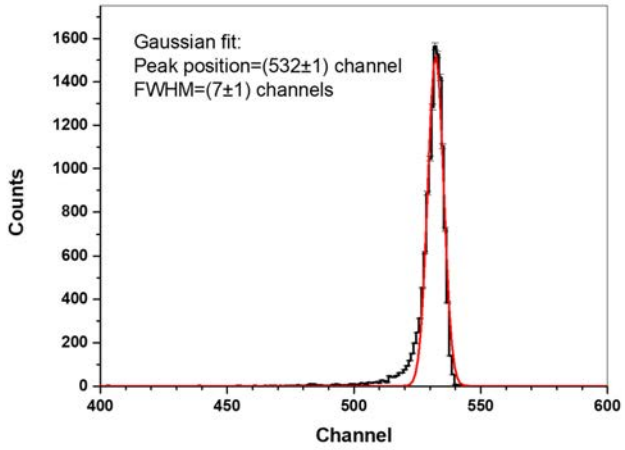

FIG. 11. Pulse height spectrum obtained using 3 MeV protons at full depletion conditions and at a bias voltage of 35 V. The red solid curve is the Gaussian fit of the experimental data. FWHM: full width at half-maximum.

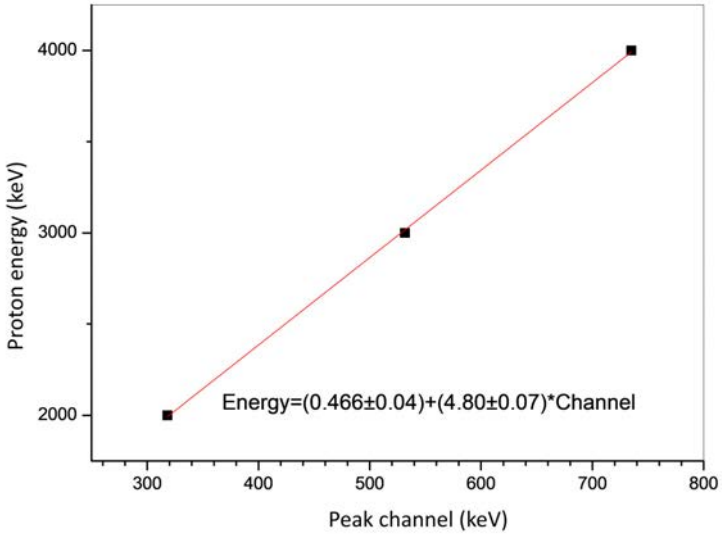

FIG. 12. Energy calibration of the electronic chain.

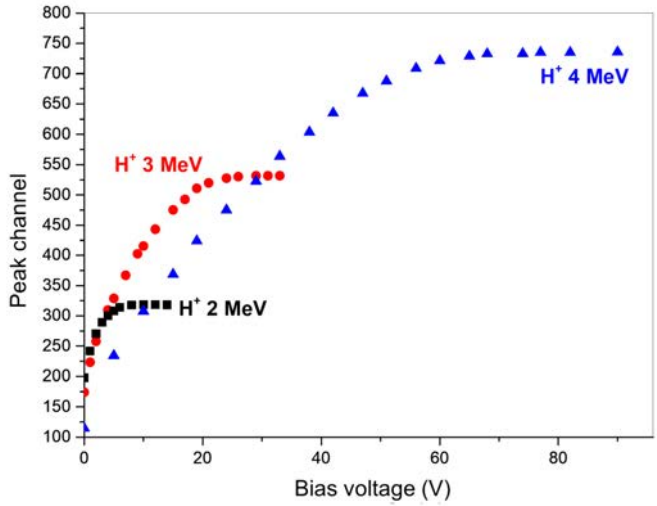

FIG. 13. Peak position versus applied bias voltage, measured using protons at different energies.

and an average energy of 3.6 eV to create and electron–hole pair in silicon [59]. The full width at half-maximum of the peak in Fig. 11 is seven channels, which, according to the previous calibration, corresponds to 33.6 ± 0.4 keV in silicon (i.e. a spectral resolution of 9300 electrons).

4.2.3. Layer thickness measurement

The effective entrance window (or dead layer) thickness can be evaluated by angle resolved IBIC analysis [38, 60, 61]. In full depletion conditions, and using weakly penetrating ions, the diode response at different angle of incidence θ decreases owing to the increase in ion path length in the dead layer of thickness t^*. The energy loss of the incident ion in the active region is given by the following equation:

$$E_{\text{loss}}(\theta) = E_{\text{ion}} - \left.\frac{\mathrm{d}E}{\mathrm{d}x}\right|_0 \frac{t^*}{\cos\theta} \tag{34}$$

where E_{ion} is the energy of the incident ion and $-\mathrm{d}E/\mathrm{d}x|_0$ is the linear stopping power at the surface. In full depletion conditions, assuming that all the carriers generated in the depletion region induce a charge that is fully collected and measured, the difference between the measured pulse height $Q^*(\theta)$ for angle of

incidence θ and the the pulse height $Q_0 = Q^*(\theta = 0)$ for angle 0, normalized with Q_0 is given by the following expression:

$$\frac{\Delta Q^*(\theta)}{Q_0} = \frac{Q^*(\theta) - Q^*(\theta = 0)}{Q^*(\theta = 0)} = \frac{1}{E_{\text{ion}}} \frac{\mathrm{d}E}{\mathrm{d}x}\bigg|_0 t^* \times \left(1 - \frac{1}{\cos\theta}\right) \tag{35}$$

Figure 14 shows a scheme of the experimental set-up. To evaluate the effective dead layer thickness of DUS1, 2.28 MeV Li ions were used and the sample was reverse biased at 20 V. Because the ion range of Li ions is 5.2 μm and the depletion layer width is about 60 μm, the full depletion conditions were effectively met; this means that the generated charge could be fully collected at sufficiently high applied bias (see Section 4.2.3).

Figure 15 shows the results of a series of IBIC measurements as the angle of incidence is varied; the same data are also shown as a function of 1−(1/cosθ). From Eq. (35), the slope of the linear fit (0.0407 ± 0.0008) is equal to $(1/E_0)t^*\mathrm{d}E/\mathrm{d}x|_0$. From the SRIM simulation, the electronic stopping power of 2.28 MeV Li ions in silicon is $\mathrm{d}E/\mathrm{d}x|_0$ = 513 eV/nm; therefore, the effective thickness of the dead layer is t^* = 180 nm. This value is considered as the effective thickness in silicon, which includes both the top oxide layer (around 110 nm, as measured by Rutherford backscattering) and the thickness in silicon immediately beneath the electrode (p^+ layer), in which charge collection is inefficient (i.e. the generated charge carriers do not contribute to the CCE).

4.3. ION MICROBEAMS

4.3.1. Set-up for ion beam induced charge technique and scanning transmission ion microscopy

Figure 14 shows a schematic representation of a typical microbeam set-up: a megaelectronvolt energy ion beam from an accelerator is focused by a system of electromagnetic quadrupole lenses and scanned over the sample surface using two sets of magnetic or electrostatic plates. The inset on the right side shows the irradiation and IBIC measurements performed in frontal IBIC geometry. Each incident ion generates a measurable charge pulse, which is amplified and processed by a standard charge sensitive electronic chain. The data acquisition system acquires and stores every event, along with the coordinates of the ion beam [54]. In an IBIC or scanning transmission ion microscopy experiment, typical ion currents are of the order of femtoampere (corresponding to a rate of less than 10^4 ions/s), which are compatible with the maximum data acquisition rate available with most microprobes [62, 63]. The experimental data are

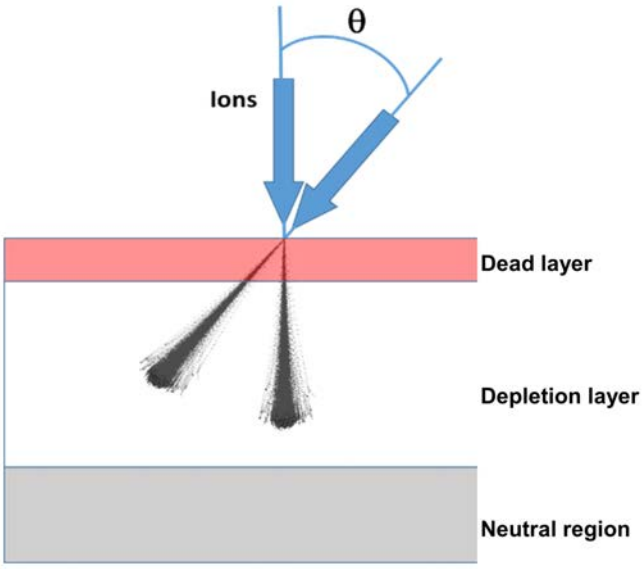

FIG. 14. Scheme of the angle resolved ion beam induced charge experiment to evaluate the entrance window thickness.

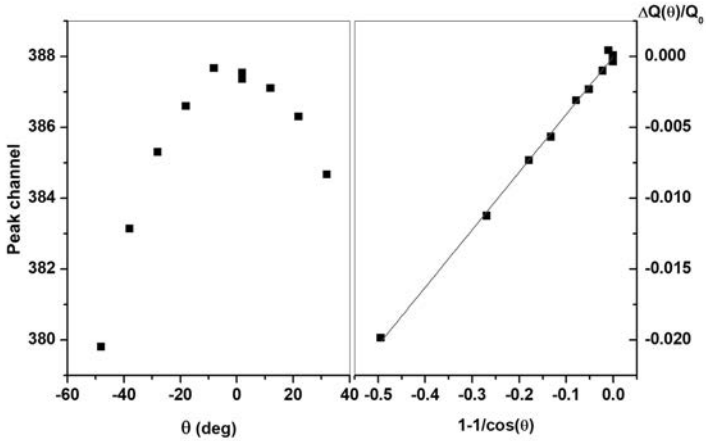

FIG. 15. Left: peak channel versus tilt angle; right: experimental data and linear fit using Eq. (35).

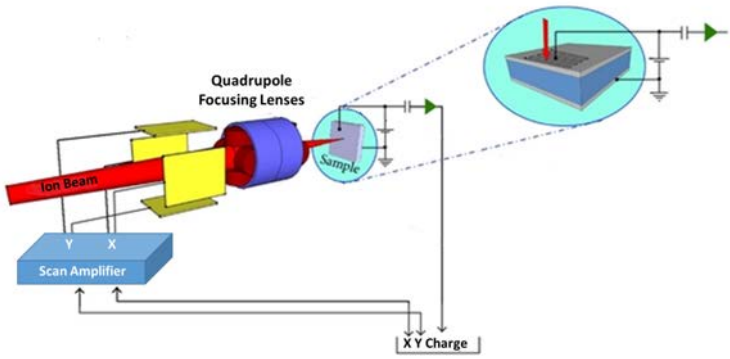

FIG. 16. Schematic representation of a typical ion microbeam set-up. Image adapted from Ref. [37] (figure licensed under CC BY 3.0).

often displayed as the mean channel number acquired in each pixel, colour or greyscale coded on a map of pixel positions; for an example, see Fig. 16.

4.3.2. Beam size and scan size determination

The usual procedure to determine the spatial resolution and the dimensional scale of the scanning region is to acquire the on-axis scanning transmission ion microscope image of a transmission electron microscopy grid with a known period, mounted in line (i.e. on top of a reference detector). A typical reference detector is DUS1.

Figure 17 shows the on-axis scanning transmission ion microscope image of a 2000 mesh (period 12.5 μm) transmission electron microscopy grid mounted on DUS1 using 8 MeV He ions. The scan area and beam spot size are calculated by fitting a line scan of the high energy peak to the theoretical profile. Figure 18 shows the line profile in one direction and the fit; the inset shows the pulse height spectrum, where the lower channel number (i.e. lower energy) peak corresponds to the wires (green in Fig. 17) and the higher channel number (i.e. higher energy) peak corresponds to the gaps in the grid (red in Fig. 17). The counts between the two peaks are due to the walls not being exactly vertical but slightly tapered. The scan area determination with this method gives an error of about 2%. The beam spot size is about 1×2 μm^2 as calculated by the slope of the line scans (in both the horizontal and vertical directions).

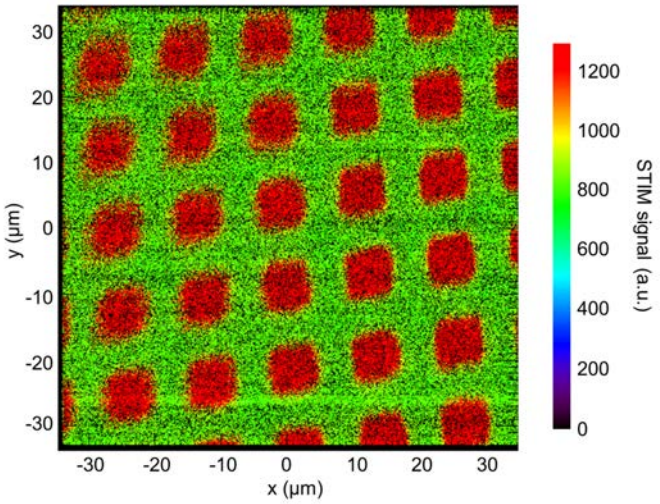

FIG. 17. Scanning transmission ion microscope image of a 2000 mesh transmission electron microscopy grid using 8 MeV He ions (image reproduced from Ref. [64]). STIM: scanning transmission ion microscope; a.u.: arbitrary units.

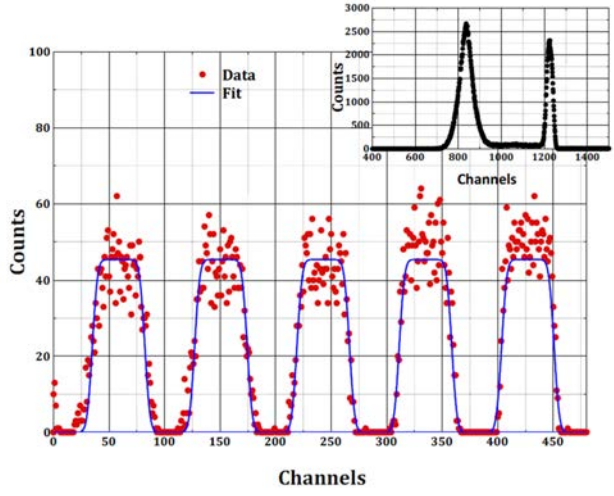

FIG. 18. Horizontal line scan of the scanning transmission ion microscope image in Fig. 17 at the high energy peak. The inset shows the ion beam induced charge spectrum (image reproduced with permission from Ref. [64]).

4.3.3. Beam current measurement

Typically, the damaged regions in this work had an area of 100 × 100 μm^2 (DUS1). DIBs scanned these regions at increasing fluences. Since the analysis (presented in Section 5) is valid in low damage conditions, the maximum DIB fluence should not induce a CCE degradation, resulting in a CCE of less than 70%.

The ion fluence is calculated by dividing the number of pulses by the surface area of the irradiated region. If standard IBIC conditions are adopted (ion currents of the order of 1 fA), the irradiation can be unacceptably slow; for example, with an ion current of 1 fA (corresponding to an ion rate of 6250 ions/s) and singly ionized DIBs, the time needed to irradiate 100 × 100 μm^2 with a fluence of 10^4 ions/μm^2 exceeds 4 h.

However, pulse height analysis and acquisition of IBIC spectra are not necessarily performed during irradiation at higher ion counting rates, which may exceed the capability of the data acquisition system (i.e. irradiation at such rates may induce a significant dead time and consequently loss in the number of recorded events), increasing the inaccuracy of the total ion irradiation fluence. The ion counting accuracy at high ion rates (comparable with the inverse of the shaping time causing pile-up events) can be improved by using a transistor–transistor logic signal extracted from a shaping amplifier connected to a pulse discriminator set above the noise level and fed into a pulse counter. In this case, ion counting rates higher than 20 kHz can be easily achieved. The fluence of the above mentioned example can therefore be achieved in about 90 min; this time is scaled down to 20 min if the irradiated area is 50 × 50 μm^2. The uncertainty of the calculated fluence values (of the order of 1%) is mainly dominated by the calibration of the scanning system.

4.3.4. Application of experimental procedures

As indicated in Section 4.1, the experimental procedures used for the irradiations contain three steps, namely: (a) CCE mapping of pristine samples, (b) damaging selected areas within the samples and (c) subsequent CCE mapping of the damaged areas. These are illustrated in Fig. 19.

4.3.4.1. CCE mapping of undamaged samples

This step is used to select uniform regions that provide a uniform IBIC response and to determine the CCE value of the pristine sample. The depletion depth of this region is evaluated in order to select N non-overlapping small areas to be irradiated by DIBs at different fluences. In the experiments carried out on DUS1, the region under study had a 500 × 500 μm^2 area. The ion energy

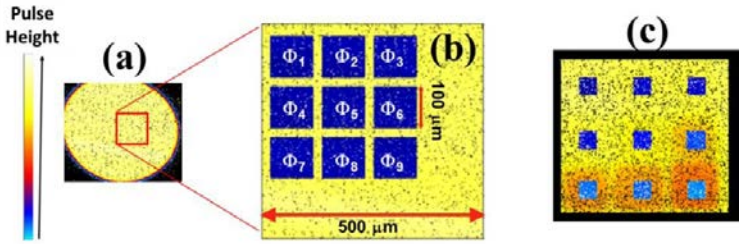

FIG. 19. (a) Uniform charge collection efficiency (CCE) image of a circular diode; no signal is received from outside the contact area. (b) Damaged regions (500 × 500 µm² area) of the diode shown in (a) and nine 100 × 100 µm² regions irradiated with fluences Φ_1, Φ_2,...., Φ_9. (c) CCE mapping of the damaged region. Image adapted with permission from Ref. [8].

and applied bias voltages for this initial step need to take into consideration the experimental settings for steps (b) and (c), as detailed in Sections 4.3.4.2 and 4.3.4.3, in order to provide the most useful comparison of the CCE before and after irradiation damage.

4.3.4.2. Damaging selected regions

The criteria adopted for the selection of the most suitable combination of probing and damaging ions can be inferred from Fig. 20, which shows, as an example, both the SRIM simulated vacancy profile for 11.25 MeV He ions in silicon [10, 16], assuming a displacement energy of 21 eV [65], and the depth (W) of the depletion region as a function of the applied bias voltage, evaluated through Eq. (4). At reverse bias voltages larger than 40 V, the entire vacancy profile is within the depletion region, whereas for lower voltages, the highly damaged region is located in the neutral region of the diode. These observations have important implications for the CCE degradation behaviour: at reverse bias voltages above 40 V, recombination occurs in the presence of a high electric field, where drift transport dominates; at low reverse bias voltages, the generation mainly affects the diffusion length of minority carriers. To apply the analytical model described in Section 5.2.1, the ion species and energies have to be chosen so that the relevant vacancy profiles fall within the depletion region corresponding to the highest allowed voltages.

4.3.4.3. Probing selected regions

The irradiated regions of the sample are then probed by PIBs using the same experimental procedures adopted in step (a) described in Section 4.3.4.1. The criteria

adopted for the selection of suitable PIBs can be inferred from a comparison of the vacancy profile and the ionization profile shown in Fig. 20.

If the PIB range is 'shallower' than the DIB (i.e. the PIB Bragg curve is shallower than the vacancy profile of the DIB in Fig. 20; e.g. PIB of 1.4 MeV He ions and DIB of 11.25 MeV He ions), only one kind of carrier (majority carriers; e.g. electrons for n-type diodes) crosses the highly damaged region, and the CCE degradation is dominated by the majority carriers' recombination. When the ionization profile covers the entire DIB range (as with 11.25 MeV He ions), both

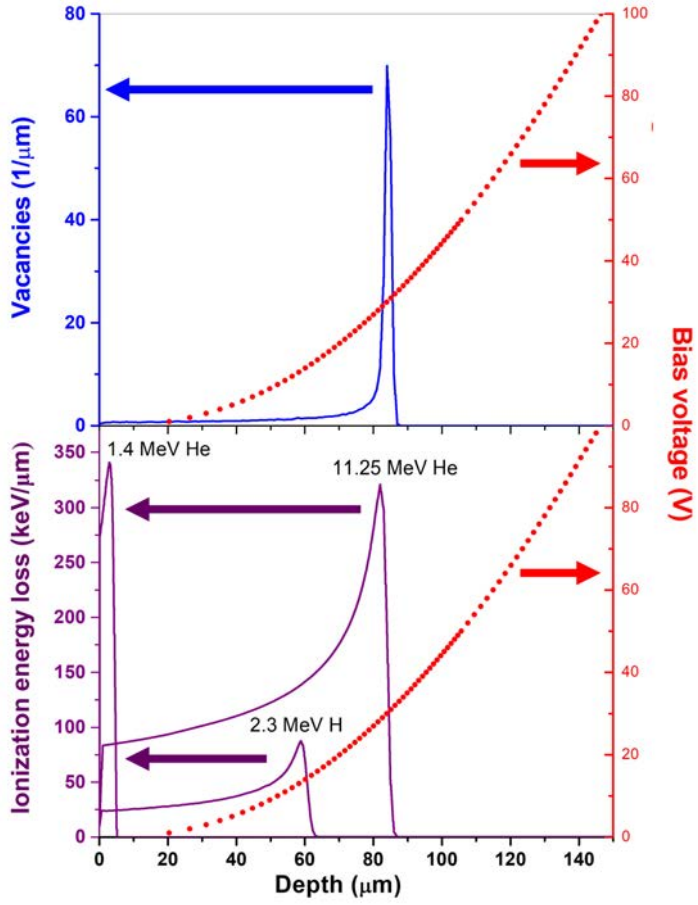

FIG. 20. Top — right axis: depletion layer width versus applied bias voltage; left axis: vacancy profile of 11.25 MeV He ions in Si, calculated by SRIM simulations. Bottom — right axis: depletion layer width versus applied bias voltage; left axis: ionization energy loss for different probing ion beams in Si, calculated by SRIM simulations.

carrier types undego recombination induced by DIB damage. If the PIB range is larger than the DIB range, the CCE degradation is dominated by minority carriers (see, for example, Ref. [20]). In the case of 2.3 MeV protons, the ionization profile covers part of the vacancy profile curve, excluding the vacancy peak; therefore, it is expected that majority carrier recombination will have a dominant, but not exclusive, role. Figure 21 summarizes the different situations occurring in fully depleted devices.

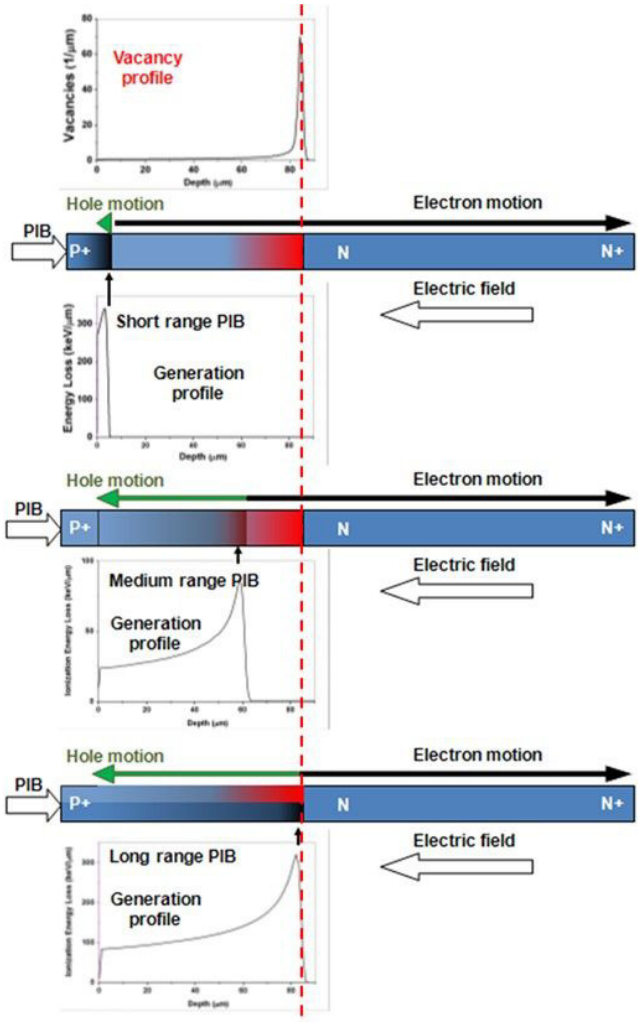

FIG. 21. Carrier motion in the depletion region compared with the generation profile (vacancy profile; top graph). PIB: probing ion beam; DIB: damaging ion beam.

CCE maps, as shown in Fig. 19, allow the damaged regions to be easily localized. The halo visible in proximity of the highest damage regions can indicate that the DIB irradiation has remarkably perturbed the effective doping of the diode. It has been previously observed that this effect induces a non-negligible perturbation of the electric field, which can modify the carrier trajectories [66]. If this effect occurs, the theoretical model described in Section 5 cannot be rigorously applied, and the analysis has to be conducted only in regions with smaller DIB fluence.

CCE maps have to be acquired at different bias voltages. This introduces an additional variable (i.e. a modulation of the electric field strength), which is included in the interpretative model and provides further information on the transport and recombination mechanisms. Again, graphic representations of the vacancy and ionization profiles (Fig. 20), combined with the depth of the depletion region as a function of bias, can be useful for selecting the appropriate bias voltage. If, for example, 2.3 MeV protons are considered as the PIB, bias voltages larger than 15 V generate depletion layers larger than the PIB range. This means that the dominant transport mechanism is carrier drift, whereas if lower bias voltages are applied, the diffusion of minority carriers generated in the neutral region has to be taken into account. Since diffusion of free carriers is, in general, a slower transport mechanism than drift, the recombination of free carriers is more effective at low bias voltage. This fact suggests that the best practice to identify the damaged area is to carry out CCE mapping at low bias voltages in order to enhance the contrast, as shown in Fig. 22, which presents the IBIC median (i.e. CCE in arbitrary units) map of a damaged region acquired at 0 V. The image clearly shows the 100 × 100 μm^2 irradiation region (square), as well as the circular region that is due to carriers diffusing into the damaged region [67, 68]. It also shows that free carriers created close to the edge of the scanned area produce full CCE. The white squares indicate the regions from which the damaged and undamaged CCE spectra are extracted.

The stabilization of radiation induced defects (i.e. the removal of transient defects in order to examine only permanent defects) can be achieved by adopting the annealing procedure prescribed in Ref. [69] (annealing at 80° for 2 h in air). However, measurements carried out 10 days after irradiation (DIB of 8 MeV He ions with fluences ranging from 1 to 1000 ions/μm^2) of the CCE degradation of DUS2 before and after annealing did not show remarkable changes and the curves overlap within errors [64].

The complete set of measurements carried out on DUS1 is shown Fig. 23. The CCE degradation curves relevant to DUS2 are reported in Ref. [20].

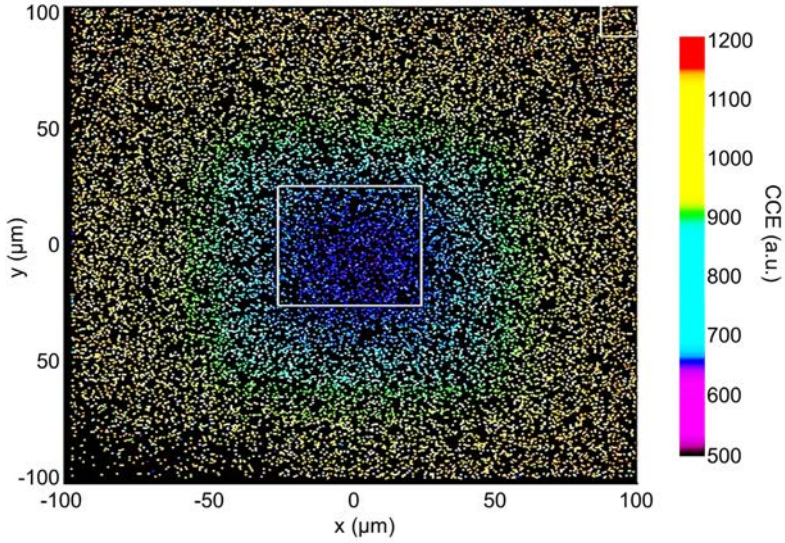

FIG. 22. Ion beam induced charge median map of DUS2 irradiated by 4 MeV He ions at 0 V (image reproduced from Ref. [64]). CCE: charge collection efficiency; a.u.: arbitrary units.

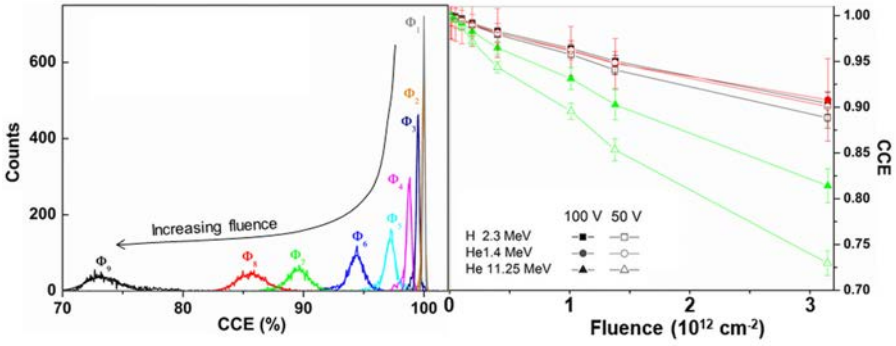

FIG. 23. Left: pulse height spectra extracted from the damaged regions (damaging ion beam of 11.25 MeV He) in DUS1, probed with a probing ion beam of 11.25 MeV He at an applied bias voltage of 50 V. Right: charge collection efficiency (CCE) centroids versus the damaging ion beam fluence, plotted for three different probing ion beams and two different applied bias voltages.

5. MODELLING OF THE CHARGE COLLECTION EFFICIENCY

This section elaborates on the modelling of the experimental results of the CCE measured by the procedure presented in Section 4.3.4 to ultimately obtain a parameter quantifying the radiation hardness.

5.1. RADIATION INDUCED CARRIER LIFETIME DEGRADATION

The modelling is based on the radiation induced recombination mechanism given by the Shockley–Read–Hall model [13] integrated with the Shockley–Ramo–Gunn theorem [31–34]. The lifetime $\tau_{e,h}^{0}$ of the pristine device is given by the following expression:

$$\frac{1}{\tau_{e,h}^{0}} = N_{e,h}^{T0}\sigma_{e,h}v_{e,h}^{th} \tag{36}$$

where $N_{e,h}^{T0}$ is the density of the recombination centres, $v_{e,h}^{th}$ is the thermal velocity and $\sigma_{e,h}$ is the electron (hole) capture cross-section. The change in the carrier lifetime, $\tau_{e,h}^{dam}$, induced by a low level of damage is given by the following equation:

$$\frac{1}{\tau_{e,h}^{dam}} = N_{e,h}^{Tdam}\sigma_{e,h}^{dam}v_{e,h}^{th} \tag{37}$$

where $N_{e,h}^{Tdam}$ is the density of recombination centres created by the DIB and $\sigma_{e,h}^{dam}$ is the corresponding electron (hole) capture cross-section of these centres.

Furthermore, under the assumption that the ratio of $N_{e,h}^{Tdam}$ to the density of vacancy interstitial Frenkel pairs is constant in depth, the concentration of active recombination centres $N_{e,h}^{Tdam}$ scales with the damaging ion fluence Φ and may be expressed as follows:

$$N_{e,h}^{Tdam}(x) = k_{e,h}\Phi\eta(x) \tag{38}$$

where $k_{e,h}$ is a factor determining the number of active traps produced per vacancy created and $\eta(x)$ is the vacancy profile (which is the number of vacancies generated per ion per unit length and is determined from SRIM/MARLOWE, as outlined in Section 3).

Defining a recombination (lifetime) damage coefficient $K_{e,h}$ as follows:

$$K_{e,h}(x) = \frac{N_{e,h}^{Tdam}(x)\sigma_{e,h}^{dam}v_{e,h}^{th}\eta(x)}{\Phi} \tag{39}$$

and using Eq. (38), it follows that:

$$K_{e,h}(x) = k_{e,h}\sigma_{e,h}^{dam}v_{e,h}^{th}\eta(x) = \alpha_{e,h}\eta(x) \tag{40}$$

where the electron (hole) capture coefficient is defined by the following expression:

$$\alpha_{e,h} = k_{e,h}\sigma_{e,h}^{dam}v_{e,h}^{th}\eta(x) \tag{41}$$

The overall lifetime degradation of the device can therefore be expressed as follows:

$$\frac{1}{\tau_{e,h}} = \frac{1}{\tau_{e,h}^{0}} + \frac{1}{\tau_{e,h}^{dam}} = \frac{1}{\tau_{e,h}^{0}} + \alpha_{e,h}\eta(x)\Phi \tag{42}$$

Thus, the effect of radiation damage can be integrated into the radiation damage model by assuming the proportionality of the recombination centre concentration $N_{e,h}^{Tdam}$ and the concentration of Frenkel pairs created immediately after irradiation, as can be calculated from binary collision approximation codes such as SRIM [16] (Assumption VII). Interactions between defects formed by multiple cascades are not taken into account. The electron (hole) capture coefficient ($\alpha_{e,h}$) is considered as a measure of radiation hardness. The model described below estimates $\alpha_{e,h}$ from the CCE measurements.

The cumulative effect of multiple scans of the region of interest to create each damage structure is a uniform cross-sectional areal distribution of the defects that are eventually formed. Therefore, the generation of vacancies occurs mainly along the ion track, along the direction normal to the irradiated electrode (i.e. x direction). The vacancy profile shown in Fig. 20 can then be used to evaluate the lifetime profiles. Figure 24 shows the electron lifetime in DUS1 as a function of the fluence Φ of the DIB (11.25 MeV He ions), assuming a capture coefficient of $\alpha_e = 2500\ \mu m^3/s$.

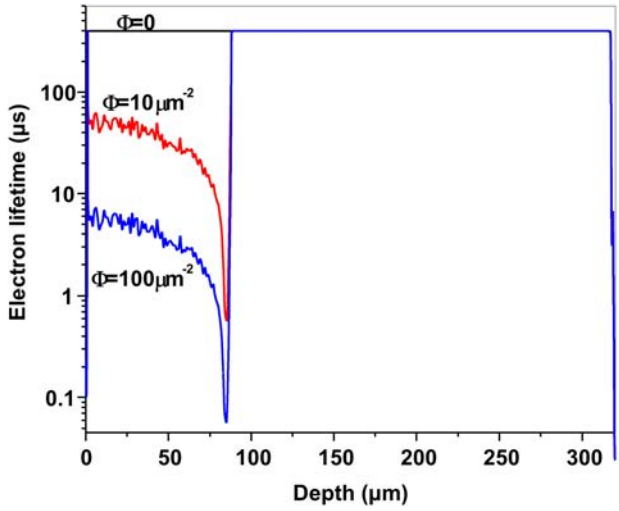

FIG. 24. Electron lifetime in DUS1 in the pristine diode (Φ = 0) and when irradiated with 11.25 MeV He ions at fluences of Φ = 10 μm^{-2} and Φ = 100 μm^{-2}.

5.2. A GENERAL MODEL FOR CHARGE COLLECTION EFFICIENCY DEGRADATION IN LOW DAMAGE CONDITIONS

The equations in Section 2 relate to the induced charge generated by a single elementary charge moving inside the semiconductor. However, to model the experiment described in Section 4.3.4, the generation profile of the PIB — which follows the Bragg curve, as shown in Fig. 20 — must be accounted for. The nuclear energy loss of megaelectronvolt energy light ions is small, so the energy spent by the ion in electronic collisions results in the creation of electron–hole pairs, and the carrier generation volume can be assumed to be a function of the x coordinate only and to be nearly cylindrical with a diameter of tens of nanometres [9].

The specific ion energy loss is then equivalent to the electronic stopping power (i.e. the amount of energy lost by the particle per unit length of its track), which is related to the generation profile through the average energy ε_{ehp} (in silicon ε_{ehp} = 3.6 eV [59]) that is necessary to create an electron–hole pair in a given semiconductor at a given temperature. ε_{ehp} is almost independent of the type and the energy of the ionizing radiation, and thus the following applies:

$$\Gamma(x) = \frac{1}{\varepsilon_{\text{ehp}}} \frac{\mathrm{d}E_{\text{ion}}}{\mathrm{d}x} \tag{43}$$

where $\Gamma(x)$ is the charge carrier generation profile (i.e. the average number of electron–hole pairs generated by ionization per unit path length).

The total induced charge at the sensing electrode produced by a single probing ion of energy E_{ion} is then given by the superposition of the contributions of any carrier generated along the ion trajectory, that is, by the convolution of the generation profile $\Gamma(x)$ and the charge induced by a single carrier moving inside the semiconductor (described by Eq. (30)), as follows:

$$Q(x,t) = q\int_0^d \Gamma(x)\left[n^+(x) + p^+(x)\right]\mathrm{d}x \tag{44}$$

The CCE is given by the ratio of the induced charge Q and the total charge generated by ionization:

$$\text{CCE} = \frac{Q}{Q_0} = \frac{\int_0^d \Gamma(x)\left[n^+(x) + p^+(x)\right]\mathrm{d}x}{\int_0^d \Gamma(x)\mathrm{d}x} = \int_0^d \gamma(x)\left[n^+(x) + p^+(x)\right]\mathrm{d}x \tag{45}$$

where $\gamma(x)$ is the normalized generation profile, defined as follows:

$$\gamma(x) = \frac{1}{E_{\text{ion}}} \frac{\mathrm{d}E_{\text{ion}}}{\mathrm{d}x} \tag{46}$$

Equation (45) is the final expression resulting from the model described above, which is suitable to interpret and fit the experimental CCE degradation shown, for example, in Fig. 23. The model entails the following step by step procedure: firstly, the solution of the continuity (Eq. (11)) and Poisson (Eq. (12)) equations to evaluate the electrostatics of the device (i.e. the electric field E and the Gunn field E^+) and the drift velocity profiles (v_{e} and v_{h}) through Eq. (71). Secondly, the solution of the adjoint continuity equation (Eq. (31)) to evaluate the CCE from a single electron–hole pair, as follows:

$$\begin{cases} \dfrac{\mathrm{d}}{\mathrm{d}x}\left(D_{\mathrm{e}} \dfrac{\mathrm{d}n^{+}}{\mathrm{d}x} \right) + v_{\mathrm{e}} \dfrac{\mathrm{d}n^{+}}{\mathrm{d}x} - n^{+}\left[\dfrac{1}{\tau_{\mathrm{e}}^{0}} + \alpha_{\mathrm{e}} \eta(x) \Phi \right] - {v_{\mathrm{e}}}^{+} - \dfrac{\mathrm{d}}{\mathrm{d}x}\left({D_{\mathrm{e}}}^{+} \right) = 0 \\ \dfrac{\mathrm{d}}{\mathrm{d}x}\left(D_{\mathrm{h}} \dfrac{\mathrm{d}p^{+}}{\mathrm{d}x} \right) + v_{\mathrm{h}} \dfrac{\mathrm{d}p^{+}}{\mathrm{d}x} - p^{+}\left[\dfrac{1}{\tau_{\mathrm{h}}^{0}} + \alpha_{\mathrm{h}} \eta(x) \Phi \right] + {v_{\mathrm{h}}}^{+} + \dfrac{\mathrm{d}}{\mathrm{d}x}\left({D_{\mathrm{h}}}^{+} \right) = 0 \end{cases} \tag{47}$$

with the relevant homogeneous boundary conditions (Eq. (32)). Thirdly, the knowledge of the vacancy profile $\eta(x)$ resulting, for example, from the SRIM simulation (as in Fig. 15). Finally, the determination of the normalized generation profile $y(x)$, for example, through the SRIM simulation (as shown in Fig. 20).

Figure 25 shows the CCE profiles of electrons (n^{+}) and holes (p^{+}) in DUS1, biased at 50 V for different levels of damage induced by a DIB of 11.25 MeV He ions, assuming that $\alpha_{\mathrm{e}} = \alpha_{\mathrm{h}} = 9000$ cm^3/s. It is apparent that with increasing fluence the recombination rate increases, resulting in a drop in the CCE profiles near the vacancy peak (see Fig. 20). The capture coefficients $\alpha_{\mathrm{e,h}}$ are therefore the free parameters, which can be extracted by fitting the CCE experimental data with Eq. (45).

5.2.1. Charge collection efficiency under full depletion conditions

Considering that in the experimental conditions presented in Section 4 all carrier generation and recombination processes occur within the depletion region of a device (Assumption VIII), the dominant charge transport mechanism is the carrier drift caused by the applied electric field, which is perpendicular to the electrodes. The Gunn weighting potential is equivalent to the weighting potential introduced by the Shockley–Ramo theorem, if charge carrier generation, transport and recombination are considered only in the depleted region (i.e. diffusion is negligible) [20, 35], as follows:

$$E^{+} = \frac{1}{W} \tag{48}$$

in the specific case of a reverse biased diode with a depletion layer width of W.

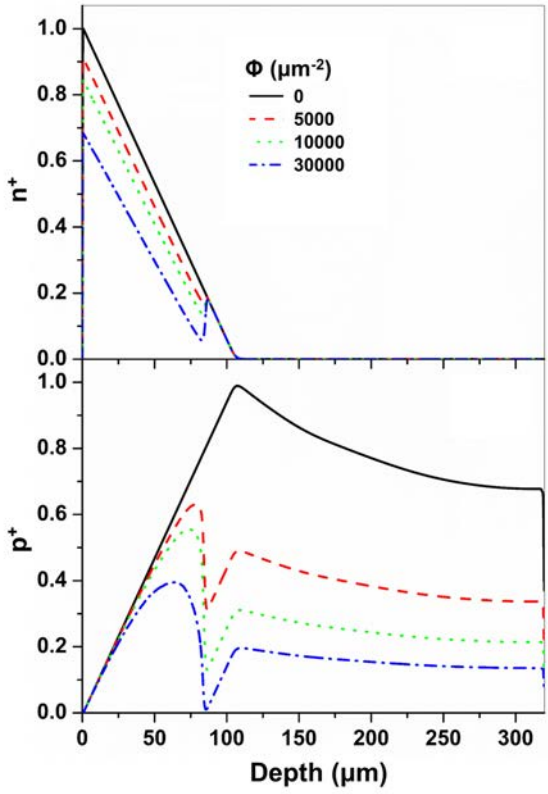

FIG. 25. Charge collection efficiency contribution of electrons (n^+; top) and holes (p^+; bottom) in DUS1 polarized at 50 V; the damaging ion beam is 11.25 MeV He at different fluences and $\alpha_h = \alpha_h = 9000\ \mu m^3/s$.

In the following, only the one dimensional geometry shown in Fig. 10 is considered. The cathode is located at $x = 0$, and the anode located at $x = d$ is grounded. In these conditions, the stationary adjoint equation Eq. (31) can be rewritten as follows:

$$\begin{cases} v_{\mathrm{e}} \dfrac{\mathrm{d}n^+}{\mathrm{d}x} - n^+ \left[\dfrac{1}{\tau_{\mathrm{e}}^0} + \alpha_{\mathrm{e}} \eta(x) \Phi \right] - v_{\mathrm{e}} E^+ = 0 \\ v_{\mathrm{h}} \dfrac{\mathrm{d}p^+}{\mathrm{d}x} - p^+ \left[\dfrac{1}{\tau_{\mathrm{h}}^0} + \alpha_{\mathrm{h}} \eta(x) \Phi \right] + v_{\mathrm{h}} E^+ = 0 \end{cases} \tag{49}$$

with boundary conditions as in Section 2.6 (see Eq. (32)).

The solution of Eq. (49) is given by the following expressions [20]:

$$\begin{cases} n^{+}(x) = \int_{x}^{d} \mathrm{d}y E^{+}(y) \exp\left[-\int_{x}^{y} \mathrm{d}z \left(\dfrac{1}{v_{\mathrm{e}}(z)\tau_{\mathrm{e}}^{0}(z)} + \alpha_{\mathrm{e}} \dfrac{\eta(z)}{v_{\mathrm{e}}(z)} \Phi \right) \right] \\ p^{+}(x) = \int_{0}^{x} \mathrm{d}y E^{+}(y) \exp\left[-\int_{y}^{x} \mathrm{d}z \left(\dfrac{1}{v_{\mathrm{h}}(z)\tau_{\mathrm{h}}^{0}(z)} + \alpha_{\mathrm{h}} \dfrac{\eta(z)}{v_{\mathrm{h}}(z)} \Phi \right) \right] \end{cases} \tag{50}$$

The total induced charge collected at the sensing electrode can be calculated using Eq. (44) and the resulting CCE is given by Eq. (45) as follows:

$$\begin{aligned} \mathrm{CCE} = \int_{0}^{d} \mathrm{d}x \gamma(x) \times \Bigg\{ & \int_{x}^{d} \mathrm{d}y E^{+}(y) \exp\left[-\int_{x}^{y} \mathrm{d}z \left(\frac{1}{v_{\mathrm{e}}(z)\tau_{\mathrm{e}}^{0}(z)} + \alpha_{\mathrm{e}} \frac{\eta(z)}{v_{\mathrm{e}}(z)} \Phi \right) \right] \\ & + \int_{0}^{x} \mathrm{d}y E^{+}(y) \exp\left[-\int_{y}^{x} \mathrm{d}z \left(\frac{1}{v_{\mathrm{h}}(z)\tau_{\mathrm{h}}^{0}(z)} + \alpha_{\mathrm{h}} \frac{\eta(z)}{v_{\mathrm{h}}(z)} \Phi \right) \right] \Bigg\} \end{aligned} \tag{51}$$

Furthermore, if the pristine diode (i.e. $\Phi = 0$) is assumed (Assumption IX) to have a CCE of 100% (i.e. the drift time is much shorter than the carrier lifetime, $1/\left\lfloor v_{\mathrm{e,h}}(z)\tau_{\mathrm{e,h}}^{0}(z) \right\rfloor \to 0$), then the CCE expression reduces to the following:

$$\begin{aligned} \mathrm{CCE} = \int_{0}^{d} \mathrm{d}x \gamma(x) \times \Bigg\{ & \int_{x}^{d} \mathrm{d}y E^{+}(y) \exp\left[-\int_{x}^{y} \mathrm{d}z \left(\alpha_{\mathrm{e}} \frac{\eta(z)}{v_{\mathrm{e}}(z)} \Phi \right) \right] \\ & + \int_{0}^{x} \mathrm{d}y E^{+}(y) \exp\left[-\int_{y}^{x} \mathrm{d}z \left(\alpha_{\mathrm{h}} \frac{\eta(z)}{v_{\mathrm{h}}(z)} \Phi \right) \right] \Bigg\} \end{aligned} \tag{52}$$

As described in Section 2, E^{+} and $v_{\mathrm{e,h}}$ are given by the electrostatic analysis of the device (see, for example, Figs 5 and 6) and the vacancy ($\eta(x)$) and normalized generation ($y(x)$) profiles can be extracted, for example, from SRIM simulations, as discussed earlier in this section and in Section 4.3.4. Equation (52) provides a simplification of Eq. (45) if Assumption VIII and Assumption IX are met.

The validity of the expression is demonstrated in Fig. 26, which shows a comparison of the analytical solution given by Eq. (52) with the numerical solution of the adjoint equation obtained with a finite element code [70].

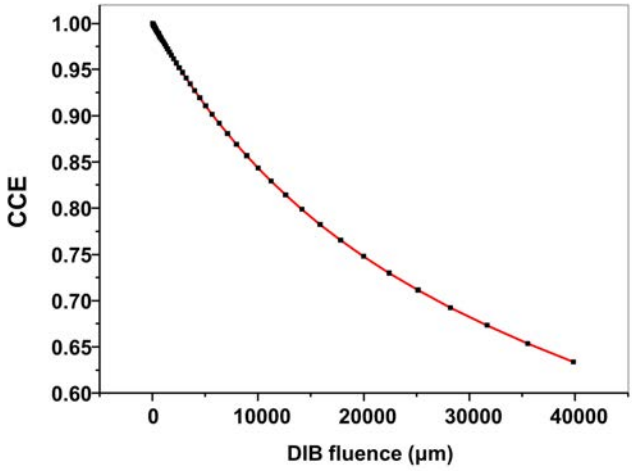

FIG. 26. Comparison of the numerical solution (black markers) of Eq. (45) with the semianalytical expression (red line; Eq. (52)). Data shown are for DUS1, with a damaging ion beam (DIB) of 11.25 MeV He, a probing ion beam of 1.4 MeV He, V = 50 V and $\alpha_e = \alpha_h$ = 9000 μm³/s.

5.2.2. Charge collection efficiency for a very low level of damage

In the case of very low levels of damage (Assumption X), which is defined as the DIB fluence range in which the CCE degradation follows a linear trend, the exponentials in Eq. (52) can be expanded into a Taylor series, providing the following approximate expression:

$$\mathrm{CCE} = \int_0^d \mathrm{d}x\gamma(x) \times \left[\int_x^d \mathrm{d}y E^+(y) \left(1 - \alpha_\mathrm{e} \Phi \int_x^y \mathrm{d}z \frac{\eta(z)}{v_\mathrm{e}(z)} \right) + \int_0^x \mathrm{d}y E^+(y) \left(1 - \alpha_\mathrm{h} \Phi \int_y^x \mathrm{d}z \frac{\eta(z)}{v_\mathrm{h}(z)} \right) \right] \tag{53}$$

$$
\begin{aligned}
&= 1 - \Phi \int_0^d \mathrm{d}z\, \eta(z) \times \left[\alpha_\mathrm{e} \frac{1}{v_\mathrm{e}(z)} \int_z^d \mathrm{d}y E^+(y) \int_0^z \mathrm{d}x \gamma(x) \right. \\
&\qquad \left. + \alpha_\mathrm{h} \frac{1}{v_\mathrm{h}(z)} \int_0^z \mathrm{d}y E^+(y) \int_z^d \mathrm{d}x \gamma(x) \right] \\
&= 1 - \Phi \int_0^d \mathrm{d}x \gamma(x) \times \left[\alpha_\mathrm{e} \int_x^d \mathrm{d}y E^+(y) \int_x^y \mathrm{d}z \frac{\eta(z)}{v_\mathrm{e}(z)} \right. \\
&\qquad \left. + \alpha_\mathrm{h} \int_0^x \mathrm{d}y E^+(y) \int_y^x \mathrm{d}z \frac{\eta(z)}{v_\mathrm{h}(z)} \right]
\end{aligned}
\tag{53}
$$

Here, the following definition has been adopted:

$$
\int_0^d \gamma(x)\,\mathrm{d}x = \int_0^d E^+(y)\,\mathrm{d}y = 1 \tag{54}
$$

Equations (53) and (54) provide evidence for the different roles played by the two carriers. To simplify, let us consider a vacancy profile localized at $x = x_0$ (i.e. $\eta(x) = V_{\mathrm{vac0}}\,\delta(x - x_0)$). If the generation profile extinguishes at depth $x < x_0$, i.e. $y(x) = \Theta(x - x_0)$, where Θ is the Heaviside step function [71], it is apparent that only electrons, which travel from 0 to d, cross the damaged region and might undergo recombination. By contrast, recombination and trapping of holes moving in the opposite direction, towards the front electrode, and crossing the low damage layer corresponding to the tail of the vacancy distribution, is negligible because the holes do not cross the highly damaged region. This simple consideration provides the basis of the experimental procedures described in Section 4.3.4, which allow the recombination and trapping of both types of charge carriers (electrons and holes) that contribute to the CCE degradation to be distinguished [20]. Moreover, if shallow PIBs are considered, the generation profile $y(x)$ extinguishes at a very short distance from the surface. In this case (single carrier charge induction), the hole contribution (the second term in the square bracket in the last expression of Eq. (53)) is negligible and the CCE expression is simplified to the following expression:

$$
\mathrm{CCE} \approx 1 - \Phi \alpha_\mathrm{e} \int_0^d \frac{\eta(z)}{v_\mathrm{e}(z)} \varphi^+(z)\,\mathrm{d}z = 1 - \alpha_\mathrm{e} \Phi^* \tag{55}
$$

The nested triple integrals in Eq. (52) collapse into a single integral, which involves both the drift velocity of the majority carriers ($v_\mathrm{e}(z)$), the vacancy

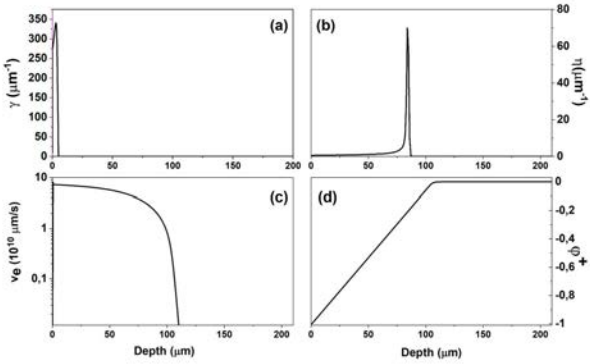

FIG. 27. (a) Normalized ionization profile of a probing ion beam of 1.4 MeV He. (b) Vacancy profile generated by a damaging ion beam of 11.25 MeV He ions in DUS1 (from a SRIM simulation). (c) Electron drift velocity in DUS1 at an applied bias voltage of 50 V. (d) Gunn weighting potential in DUS1 at the same applied bias voltage.

profile ($\eta(z)$) and the electrostatics of the device through the Gunn weighting potential $\varphi^{+}(z)$.

This is the case for 1.4 MeV He ions probing the damage induced by 11.25 MeV He ions in DUS1. The profiles of these quantities are shown in Fig. 27 for a bias voltage of 50 V.

Under the assumption of very shallow PIBs, the CCE degradation as a function of the DIB fluence follows a linear trend. The term Φ^{*} in Eq. (55) is the effective DIB fluence, defined as follows:

$$\Phi^{*} = \Phi \int_{0}^{d} \frac{\eta(z)}{v_{\mathrm{e}}(\mathrm{z})} \varphi^{+}(z)\,\mathrm{d}z \tag{56}$$

The slope of the linear fit of the experimental data plotted as a function of Φ^{*} provides the capture coefficient α_{e} (see Fig. 28).

5.2.3. The displacement damage dose

In the case of a low level of damage, Eq. (53) correlates this model with the approach based on the 'displacement damage dose' proposed in Ref. [4], as described in Ref. [20]. By adopting Assumption XI, a constant vacancy profile is obtained up to a depth of $R^{\mathrm{d}} < d$:

$$\eta(x) = \theta\left(R^{\mathrm{d}} - x\right) \times \frac{V_{\mathrm{T}}}{R^{\mathrm{d}}} \tag{57}$$

where V_{T} is the total number of vacancies, that is, $\eta(x)$ is the constant average value of the vacancy profile. The linear degradation of CCE can be expressed as follows:

$$\mathrm{CCE} = 1 - \Phi \frac{V_{\mathrm{T}}}{R^{\mathrm{d}}} \int_0^d \mathrm{d}z \left[\alpha_{\mathrm{e}} \frac{1}{v_{\mathrm{e}}(\mathrm{z})} \int_z^d \mathrm{d}y E^+(y) \int_0^z \mathrm{d}x \gamma(x) + \alpha_{\mathrm{h}} \frac{1}{v_{\mathrm{h}}(z)} \int_0^z \mathrm{d}y E^+(y) \int_z^d \mathrm{d}x \gamma(x) \right] \tag{58}$$

This expression can be connected to the phenomenological concept of the displacement damage dose, D_{d} [4]. The displacement damage dose is defined as the displacement damage energy deposition per unit mass of material and can be calculated as the product of the particle fluence and the respective NIEL of the particle. In the framework of the NIEL theory, the CCE decreases with the accumulated displacement damage dose through the following simple expression:

$$\mathrm{CCE} = 1 - K_{\mathrm{ed}} \times D_{\mathrm{d}} \tag{59}$$

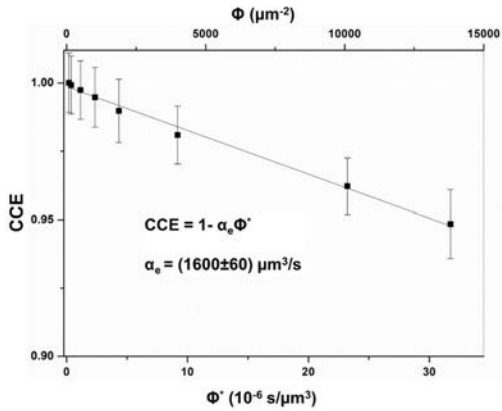

FIG. 28. Charge collection efficiency (CCE) degradation of DUS1 (at an applied bias voltage of 50 V) induced by 11.25 MeV He ions and probed with 1.4 MeV He ions as a function of fluence (top horizontal axis) and of effective fluence (bottom horizontal axis). The line represents the linear fit of the data at low fluence.

where K_{ed} is the equivalent damage factor defining the rate of linear decrease. The displacement damage dose D_d is defined as follows [4]:

$$D_d = \left(\frac{\varepsilon_{Vac}}{\rho_M} \times \frac{V_T}{R^d} \right) \Phi \tag{60}$$

where ρ_M is the mass density of the irradiated material (2.32 g · cm^{-3} in silicon) and ε_{Vac} is the average energy necessary to produce a vacancy. The displacement damage dose can be calculated from SRIM simulations, considering the following expression:

$$\varepsilon_{Vac} = \frac{T_d}{0.4} + 2 \tag{61}$$

where 2 is added to allow for the binding energy loss that SRIM assigns to each vacancy and T_d is the threshold energy for atomic displacement. In silicon, considering a typical value of T_d = 21 eV [65], ε_{Vac} = 54.5 eV.

By comparing Eq. (59) and Eq. (53) using the definition of Eq. (60), the following analytical expression for the equivalent damage factor is obtained:

$$\begin{aligned} K_{ed} = \frac{\rho_M}{\varepsilon_{Vac}} \int_0^d \mathrm{d}z \Bigg[& \alpha_e \frac{1}{v_e(z)} \int_z^d E^+(y)\,\mathrm{d}y \int_0^z \gamma(x)\,\mathrm{d}x \\ & + \alpha_h \frac{1}{v_h(z)} \int_0^z E^+(y)\,\mathrm{d}y \int_z^d \gamma(x)\,\mathrm{d}x \Bigg] \end{aligned} \tag{62}$$

This expression explicitly shows the dependence of the equivalent damage factor K_{ed} on the following:

- The electrostatics of the device, through the Gunn field E^+;
- The carrier transport, through the drift velocities $v_{e,h}$;
- The recombination features, through the capture coefficients $\alpha_{e,h}$;
- The ion probe ionization profiles, through the normalized generation profile $\gamma(x)$.

If the experimental conditions (i.e. bias applied to the device and ion probe), as well as the ranges of the damaging ions, are maintained constant, under Assumption VIII to Assumption X, the NIEL approach can effectively correlate the CCE degradation of an electronic device induced by different radiation sources or energies, as demonstrated in Refs [7, 8]. If one or more of

these conditions are not fulfilled, the complete expression given by Eq. (44) has to be used.

5.3. DETERMINATION OF THE CAPTURE COEFFICIENTS

Data analysis of the CCE degradation curves, as illustrated in Fig. 23, is aimed at extracting the capture coefficients $\alpha_{e,h}$. The evaluation of these parameters is performed by fitting the experimental data with Eq. (45), which is derived from the general model. In general, the model involves the numerical solution of the differential equations Eq. (47), or their semianalytical solution given by Eq. (52) if Assumption VIII is met.

The highly non-linear nature of these equations and the relevant integrals prevents any analytical approach of the fitting procedure, and the following method can be adopted.

The capture coefficients can be evaluated by the least squares method [72], which is the statistical method most widely used in practical problems. It consists in the minimization, with respect to the unknown parameters α_e, α_h, of the matrix $\boldsymbol{M}$ of the sum of the squares of the residuals, normalized by the uncertainty $\sigma(i)$ of the ith measurement, as follows:

$$\boldsymbol{M}\left(\alpha_e,\alpha_h\right)=\sum_{i=1}^{N}\left[\frac{\mathrm{CCE}_{\mathrm{exper}}(i)-\mathrm{CCE}_{\mathrm{model}}(i)}{\sigma(i)}\right]^2 \tag{63}$$

that is, the sum of the squares of the difference between the experimental data and the values predicted by the model. $\mathrm{CCE}_{\mathrm{exper}}$ is the CCE data extracted from N regions (typically nine) irradiated at different fluences (see Fig. 23), $\sigma(i)$ is the uncertainty from the peak fitting of the CCE spectra, also shown in Fig. 23, and $\mathrm{CCE}_{\mathrm{model}}$ is the theoretical CCE evaluated from Eq. (45).

The function $\boldsymbol{M}(\alpha_e, \alpha_h)$ can be interpreted geometrically, since it defines a surface in three dimensional space spanned by the parameters α_e and α_h. It can be evaluated systematically by using a lattice of points over the parameter (α_e, α_h) plane and searching for the point (α_e, α_h) that yields the smallest value of $\boldsymbol{M}$. The procedure to evaluate each element of the matrix is as follows:

(a) The interval $[0, \alpha^{\mathrm{Max}}]$ of α_e and α_h is divided into a fixed number of bins. α^{Max} is arbitrarily chosen by the user on the basis of preliminary trials. In the following, the maximum value of the parameters α_e and α_h is set to $\alpha^{\mathrm{Max}} = 12\,000\ \mu\mathrm{m}^3/\mathrm{s}$. Clearly, a large parameter domain allows the absolute minimum to be identified, but an accurate fitting procedure requires a large number of bins, resulting in a high computation time.

(b) Each matrix element contains the value of the residual.
(c) The minimum of the matrix represents the combination of α_e and α_h that provides the best fit of the experimental data.
(d) The fitted curves of the CCE for different PIBs represent those using the α_e and α_h values that minimize a matrix element of $\boldsymbol{M}$.

Although this rough method can potentially lead to local minima, it has been used because (i) it is easy to implement despite the complex non-linear CCE expression in Eq. (45) and (ii) it enables the combination of multiple fitting routines.

Moreover, the physical meaning of the fitting parameters α_e and α_h can help to identify absolute minima and therefore the parameters that provide the best fit of the experimental data, as discussed at the end of this section.

To effectively implement this minimization strategy, it is opportune to start from a first rough estimate of (α_e, α_h) in order to limit the parameter space. For example, it is recommended to use the parameter relevant to the majority carriers (i.e. electrons for DUS1) obtained by using shallow PIBs, as described in Fig. 27. In this specific case, the hole contribution can be neglected and $\boldsymbol{M}$ is a function of only α_e, leading, under Assumption X, to a traditional linear fit. In general, it is recommended to extract the starting values of the parameters (defined in Eq. (41)) from the capture cross-sections of defects and using k factors (of the order of unity) available in the literature [7, 8, 20]. This systematic scanning of the parameter space to find the minimum of $\boldsymbol{M}$ is a consuming process, in terms of both time and computing resources.

It is worth noting that parameters α_e and α_h are fluence scaling factors that separately enter the equations relevant to electrons and holes, respectively. Therefore, it is possible to optimize the minimization algorithm to calculate CCE_{model} by adopting the following approach:

(a) The solution of Eq. (45) at different DIB fluences Φ is calculated separately for electrons ($CCE^{e}_{model}\left(\alpha_e^{Max}\Phi\right)$) and holes ($CCE^{h}_{model}\left(\alpha_h^{Max}\Phi\right)$) using the highest values of the parameters α_e^{Max} and α_h^{Max}, which define the boundary of the parameter space.
(b) For any coordinate of a lattice point over the region of variability of the parameter (α_e, α_h) plane, CCE^{e}_{model} and CCE^{h}_{model} are calculated at different DIB fluences by separately interpolating the $CCE^{e}_{model}\left(\alpha_e^{Max}\Phi\right)$ and $CCE^{h}_{model}\left(\alpha_h^{Max}\Phi\right)$ curves.

As an example, let us consider the case of DUS1 irradiated with a DIB of 11.25 MeV He ions, with the damage probed with a PIB of 1.4 MeV He ions (this is discussed in Section 5.2.2 for the case of a very low level of damage).

Figure 29 shows the $CCE^{e}_{model}\left(\alpha_e^{Max}\Phi\right)$ and $CCE^{h}_{model}\left(\alpha_h^{Max}\Phi\right)$ curves, calculated by numerically solving Eq. (45), using $\alpha_e^{Max} = \alpha_h^{Max} = 12\,000\ \mu m^3/s$. As expected, with the PIB having a very small range (about 5 μm), the hole contribution to the CCE is negligible (0.015) and the hole sensitivity to the much deeper damage induced by the DIB is negligible. Since the charge carrier generation curve is shallower than the damage profile, the majority carriers (electrons) drift towards the anode (located at x = 320 μm) and cross the highly damaged region located at the vacancy peak, where the recombination probability is the highest (see Fig. 24). Because the trajectories of the electrons develop along the tail of the vacancy profile, the traps induced by radiation damage very marginally influence their lifetime.

The $CCE^{e}_{model}\left(\alpha_e\Phi\right)$ curves are calculated from the interpolation of $CCE^{e}_{model}\left(\alpha_e^{Max}\Phi\right)$ at the experimental values of the fluences. The behaviour of the $\boldsymbol{M}$ function versus α_e shows that the minimum of the squared sum of residuals occurs at α_e = 1680 $\mu m^3/s$, indicating that this is the best fit to the experimental data, as shown in Fig. 30 (top left). A similar procedure can be extended to two dimensions, considering the function $\boldsymbol{M}$ in the (α_e, α_h) parametric space. The hypersurface can then be represented by a contour plot, as shown in Fig. 30 (top right). Again, the $\boldsymbol{M}$ hypersurface shows minima corresponding to α_e = 1680 $\mu m^3/s$, independent of the α_h values, since the minimum locus lies

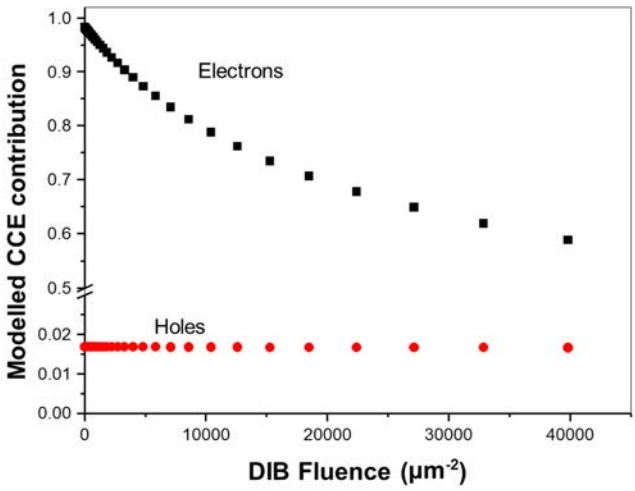

FIG. 29. Charge collection efficiency (CCE) degradation curves of electrons (CCE^{e}_{model}) and holes (CCC^{h}_{model}) for DUS1. The damaging ion beam is 11.25 MeV He ions, the probing ion beam is 1.4 MeV He ions, the applied bias voltage is 50 V and $\alpha_e = \alpha_h$ = 12 000 $\mu m^3/s$.

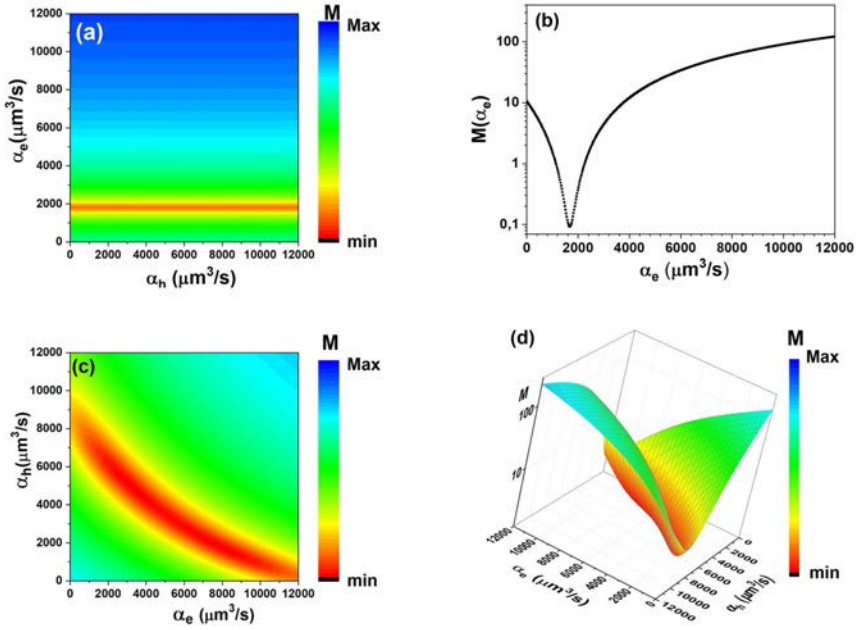

FIG. 30. Squared sum of residuals as a function of different values of α_e. *(a)* **M**(α_e, α_h) *contour plot for a damaging ion beam of 11.25 MeV He ions, a probing ion beam of 1.4 MeV He ions and an applied bias voltage of 50 V. (b) Line plot,* **M**(α_e), *of the vertical projection of the contour plot shown in (a). (c)* **M**(α_e, α_h) *contour plot for a damaging ion beam of 11.25 MeV He ions, a probing ion beam of 11.25 MeV He ions and an applied bias voltage of 50 V. (d) Three dimensional colour fill map of the* **M** *surface shown in (c).*

along a line parallel to the horizontal axis. It is worth noting that the value of α_e is close to the value calculated using the 'effective fluence' approach (see Fig. 28).

In the case of more penetrating PIBs, both carriers play a role in the degradation of the CCE. For example, considering the analysis of the CCE degradation induced by a DIB of 11.25 MeV He ions and measured using the same ions (PIB is the same as DIB), the contributions of electrons and holes to the CCE degradation are shown in Fig. 31, assuming $\alpha_e = \alpha_h = 12\,000$ μm^3/s.

Figure 30 (bottom left) shows the contour plot of the ***M*** hypersurface. It is apparent that the minimum locus spans the whole parameter space and is not parallel to the horizontal or to the vertical axis; this indicates that the best fit of the experimental data is given by a combination of both the majority and minority carrier contributions. In this specific case, the minimum of the ***M*** function is obtained for $\alpha_e = 1760$ μm^3/s and $\alpha_h = 7840$ μm^3/s, which define a theoretical CCE curve that fits the experimental data well, as shown in Fig. 32.

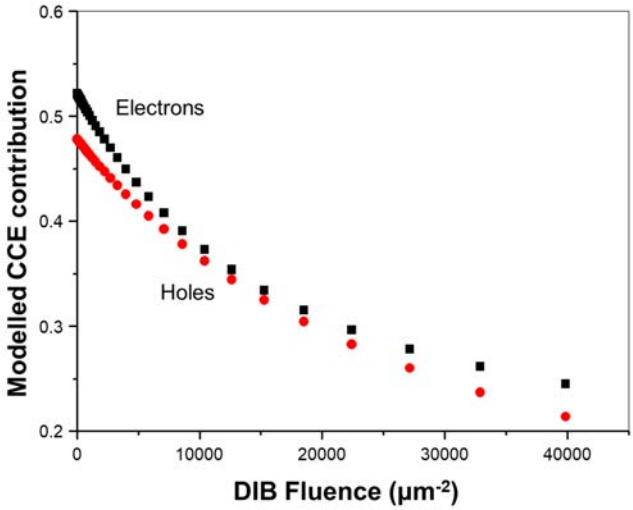

FIG. 31. Charge collection efficiency (CCE) degradation curves of electrons (CCE^{e}_{model}) and holes (CCE^{h}_{model}) for DUS1. The damaging ion beam (DIB) is 11.25 MeV He ions, the probing ion beam is 11.25 MeV He ions, the applied bias voltage is 50 V and $\alpha_e = \alpha_h$ = 12 000 μm³/s.

However, it is worth noting that the minimum locus is almost flat, as shown in the three dimensional plot of the ***M*** hypersurface; that is, the sum of the squared residuals does not vary remarkably within this hyperbolic-like minimum locus (bottom right of Fig. 30). The two measurements, carried out with different PIBs (1.4 MeV He and 11.25 MeV He) should be consistent. Therefore, the two ***M*** functions relevant to the two PIBs have been combined to extract the capture coefficients α_e, α_h that minimize the combined squared sum of residuals, that is:

$$\boldsymbol{M}_{(\mathrm{PIB1.4MeVHe})+(\mathrm{PIB11.25MeVHe})} = \boldsymbol{M}_{(\mathrm{PIB1.4MeVHe})} + \boldsymbol{M}_{(\mathrm{PIB11.25MeVHe})} \tag{64}$$

From the graphical point of view, this operation corresponds to the overlapping of the two contour plots shown in the top right and bottom left of Fig. 30. The intersection of the two minimum loci identifies a unique minimum, as shown in Fig. 33. The coordinates of the minimum are α_e = 1600 μm³/s, α_h = 8160 μm³/s; these values provide the best fit of the experimental data, as shown in Fig. 34 (right side). The same procedure can then be extended to other conditions (i.e. by adding additional data for different probe ions and bias voltage combinations).

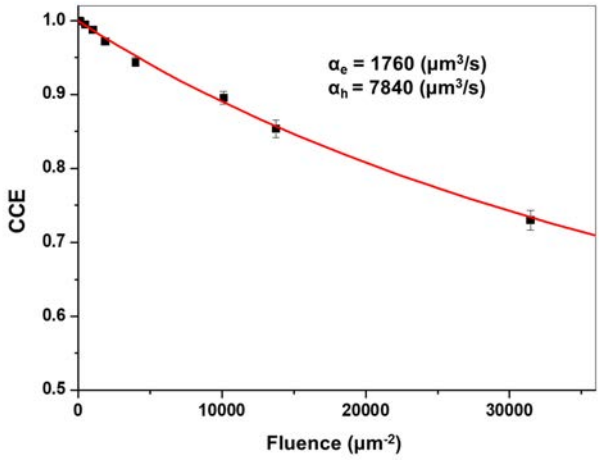

FIG. 32. Best fit (α_e = 1760 $\mu m^3/s$ and α_h = 7840 $\mu m^3/s$; continuous line) of the data (markers) for the experiment carried out on DUS1, with a damaging ion beam of 11.25 MeV He ions and a probing ion beam of 11.25 MeV He ions. CCE: charge collection efficiency.

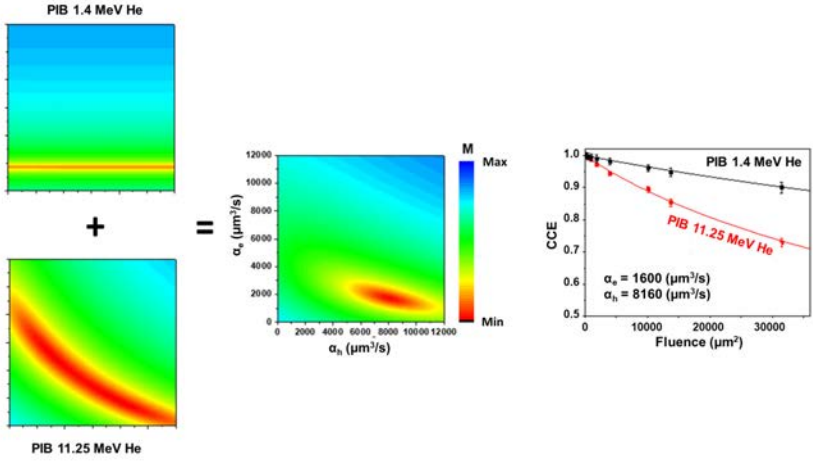

FIG. 33. Left: combination of the two residual maps relevant to two different probing ion beams (PIBs). Centre: the resulting contour plot, evaluated through Eq. (65). Right: the relevant charge collection efficiency (CCE) degradation curves. Continuous lines: calculated using α_e = 1600 $\mu m^3/s$ and α_h = 8160 $\mu m^3/s$; markers: experimental data.

The global $\boldsymbol{M}$ hypersurface is then defined as follows:

$$\boldsymbol{M}_{\text{Global}} = \sum_{i=1}^{N_{\text{PIB}}} \sum_{j=1}^{N_{\text{V}}} M_{i,j} \tag{65}$$

where N_{PIB} is the number of ion probes (in this case $N_{\text{PIB}} = 3$) and N_{V} is the number of applied bias voltages (in this case $N_{\text{V}} = 2$) used in all the experiments.

The final fitting procedure performed with the three different PIBs on the experimental CCE degradation data of DUS1 biased at 50 V and 100 V is summarized in Fig. 34. The figure shows the $\boldsymbol{M}$ function value maps extracted from the data for three different PIBs and the two bias voltages.

Finally, a map of $\boldsymbol{M}$ function values combining all experimental datasets (in this case, three PIB values for two bias voltages each) can be produced and the capture coefficients can be extracted from its minimum value. The best fit is obtained for $\alpha_e = 1520$ μm^3/s and $\alpha_e = 8320$ μm^3/s. These capture coefficients are used to calculate, through Eq. (45) or Eq. (47), the theoretical CCE degradation

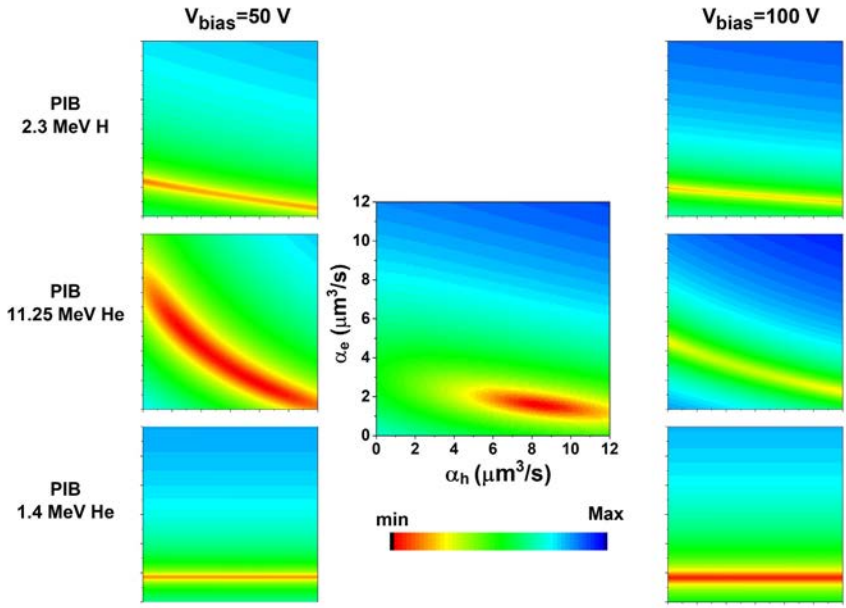

FIG. 34. Contour plots of the **M** *functions relevant to different probing ion beams (PIBs) and different bias voltages (V_{bias}). The central contour plot is the convolution of the individual* **M** *functions.*

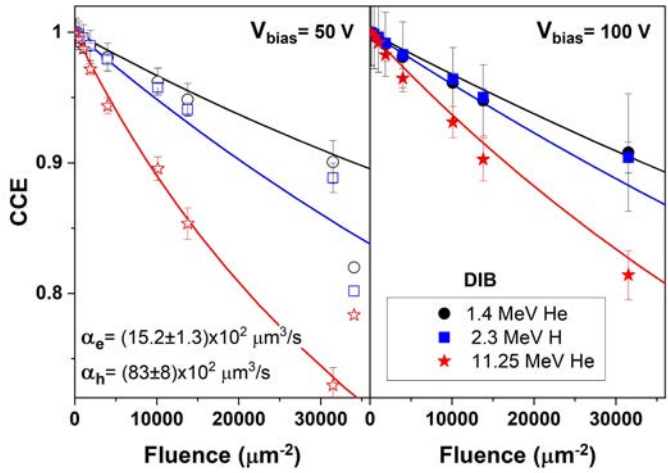

FIG. 35. Final evaluation of the capture coefficients α_e and α_h, obtained by merging the analysis carried out at 100 V (filled markers) and 50 V (open markers) with different probing ion beams and limited to fluences <2 × 10^{12} ions/cm^2. CCE: charge collection efficiency; DIB: damaging ion beam.

curves, which well fit the experimental data acquired under any experimental conditions, as shown in Fig. 35.

5.4. ERROR BUDGET

Evaluation of the measurement uncertainty is needed to complete the analysis. The uncertainty can be determined from the calculation of the error matrix **Err**, which is the inversion of the Hessian matrix $\boldsymbol{H}$ of the $\boldsymbol{M}$ function. $\boldsymbol{H}$ is the second derivative matrix of $\boldsymbol{M}$ with respect to the free parameters α_e and α_h, calculated at the best parameter values (i.e. at the minimum of the $\boldsymbol{M}$ function). The diagonal elements of the error matrix are the squares of the individual parameter errors and include the effects of correlations with the other parameters.

$$\boldsymbol{H}(\alpha_e,\alpha_h)=\begin{pmatrix} \dfrac{\partial^2 \boldsymbol{M}}{\partial \alpha_e^2} & \dfrac{\partial^2 \boldsymbol{M}}{\partial \alpha_e \partial \alpha_h} \\ \dfrac{\partial^2 \boldsymbol{M}}{\partial \alpha_e \partial \alpha_h} & \dfrac{\partial^2 \boldsymbol{M}}{\partial \alpha_h^2} \end{pmatrix} \tag{66}$$

$$\mathbf{Err}\left(\alpha_e,\alpha_h\right)=\boldsymbol{H}^{-1}\left(\alpha_e,\alpha_h\right) \tag{67}$$

The diagonal elements of the Hessian matrix contain the partial derivatives with respect to one parameter at a time and are therefore not coupled to any other parameters. However, when the matrix is inverted, the diagonal elements of the resulting error matrix contain contributions from all the elements of the Hessian matrix and determine the cross-correlations [73]. The Hessian and error matrices in this study are the following:

$$\boldsymbol{H}\left(\alpha_e,\alpha_h\right)=\begin{pmatrix} 9.59743\times10^{-5} & 1.1864\times10^{-5} \\ 1.1864\times10^{-5} & 2.52317\times10^{-6} \end{pmatrix} \tag{68}$$

$$\mathbf{Err}\left(\alpha_e,\alpha_h\right)=\begin{pmatrix} 24\,440 & -114\,163 \\ -114\,163 & 929\,612 \end{pmatrix} \tag{69}$$

This leads to the final values of α_e = 1600 ± 160 μm^3/s and α_h = 8200 ± 960 μm^3/s. The correlation coefficient is the following:

$$\mathrm{corr}=\frac{\mathrm{Err}_{12}}{\sqrt{\mathrm{Err}_{11}\times\mathrm{Err}_{22}}}=-0.758 \tag{70}$$

A short discussion about the meaning of the correlation coefficient is as follows: the model adopted to interpret the CCE degradation is based on the assumption that the induced charge is given by the independent contributions of electrons and holes (see Eq. (44)); therefore, α_e and α_h are assumed not to be correlated (i.e. the correlation coefficients should be zero). However, the final expression of the fitting curve (i.e. Eq. (47) or Eq. (53)) involves the contributions of both carriers, which have common terms given by the normalized charge generation profile γ (Eq. (46)) and the vacancy distribution used in the integral and in the expression of the lifetime as detailed in Section 5. Therefore, the final general expression, Eq. (47), naturally correlates the two contributions. As an example, in the case of shallow PIBs, there is no correlation between α_e and α_h because the generation profile γ makes the contribution of minority carriers negligible, whereas in the case of highly penetrating PIBs (Fig. 33, top right), both carriers play a role and the residual map clearly shows a correlation. In principle, if an additional experiment was carried out using shallow PIBs incident on the back electrode, then only the minority carriers would contribute to the CCE degradation, generating a residual map similar to that presented in the top left part of Fig. 33, but rotated by 90°. In this case, by combining the two orthogonal residual maps (one produced mainly by the contribution of electrons and the other by the contribution of holes), the resulting minimum locus will be

an axis symmetrical ellipse (i.e. with a null correlation coefficient). If PIBs of different ranges always irradiate the front electrode, as in the examples reported here, tilted ellipses (i.e. non-zero correlation coefficients) are unavoidable.

6. SUMMARY AND OUTLOOK

The IAEA's CRP F11016, involving 14 institutes from 13 Member States and running from December 2011 to November 2016, aimed at promoting the utilization of ion accelerators for studying and modelling radiation induced defects in semiconductors and insulators. One of the expected outcomes of CRP F11016 was to develop comprehensive guidelines, accessible to any laboratory equipped with ion accelerators and standard electronics for the detection of ionizing particles, for the measurement and interpretation of CCE degradation in semiconductors caused by displacement damage effects induced by ion irradiation.

This publication details both the experimental and the theoretical aspects of these guidelines. It describes in full detail each of the phases of an experiment carried out on a commercial silicon photodiode, which is commonly used in ion beam facilities as a low cost particle detector for certain applications that do not require the high energy resolution provided by the highest spectroscopic grade silicon detectors.

The core of the guidelines is based on the use of energetic ions accelerated in the megaelectronvolt energy range, which play a dual role: (i) as damaging agents to generate defects in the active semiconductor material of the electronic device (in this case, a diode) and (ii) as probes to measure the effect of low level radiation damage on the CCE, as the main feature defining the electronic response of tested or irradiated semiconductor devices. The low level radiation damage is assumed to be an accumulation of simple point defects (i.e. vacancies, interstitials, or their complexes with atoms present in the crystal lattice) created by ion cascades; the traps formed do not undergo any transformation, because of weakly overlapping cascades that are formed subsequently during the irradiation procedure. The total defect (or trap) concentration needs to be lower than the initial doping concentration in order to avoid perturbing the effective doping profile. Focused ion microbeams and the IBIC technique are used in the two phases of the experiment, which include: (i) the creation of patterned partly damaged areas covering a large range of implantation fluences and (ii) the sensing of the degradation of the CCE due to the damage created. Ions with different energy and mass provide agents and probes whose end of range can be

tuned to the region of interest, which varies with the specific operating conditions of the devices. In addition to exploiting the double nature of ions as damaging agents and probes, another advantage of using this method for the assessment and evaluation of radiation hardness in semiconductor materials is that the increase of dark current, which affects the device features, is negligible owing to the small size of the damaged region compared to the total active volume of the device. This is an important factor, which allows IBIC to be employed as the main characterization technique for the electronic features of semiconductors. The IBIC technique (including time resolved IBIC [9] and heavy ion charge transient spectroscopy [74]) is the most suitable ion beam analysis technique for functional analysis of electronic materials, has solid theoretical foundations and can be easily implemented in any nuclear microprobe facility owing to its operational simplicity.

The general model developed during CRP F11016 integrates the Shockley–Read–Hall recombination model into the Shockley–Ramo–Gunn theory (Section 2.5). The model relies on the generation of recombination centres being the only effect induced by atomic displacements that result from the interaction of the incoming ion with the atomic lattice. The resulting carrier lifetimes are connected to the ion fluence through Eqs (36–42), which give trap distribution profiles proportional to the distribution of vacancies created initially by the radiation. Moreover, it is assumed that the carrier transport properties (i.e. carrier mobilities) and the effective doping concentration (and thus the electric field) are not affected by the ion irradiation (Assumption V).

The above mentioned assumptions define the condition of 'low level of damage' adopted in this work, and the interpretative model can be effectively used only in this regime and in full depletion conditions (i.e. when the ionizing tracks of both PIBs and DIBs lie within the depletion region) (Assumption VIII).

The formulation of the model is general, and the model can in principle be adopted also in cases in which not all assumptions (summarized in Appendix I) are valid. In the case of partially depleted devices characterized by a limited depletion region and a neutral region in the bulk semiconductor material, the analytical general solution of Eq. (52) is not applicable, but the solutions of Eq. (47) can be calculated numerically. Therefore, the model can be extended also to cases of study in which the depletion region is smaller than the range of the probing and damaging ions. However, this case is not treated in this report, because it relies on more complex instrumentation and theoretical methods (see Ref. [19] for a case in which the damage affects the diffusion regime only). The mechanism of charge induction ascribable to the diffusion of minority carriers is generally much slower than the drift component. This fact is the cause of ballistic deficit effects [38], which can lead to the loss of a variable fraction of the signal if the amplifier shaping time is comparable to the rise time of the signal emerging

from the preamplifier; this can be mitigated using gated integrators, which are not often available in a standard laboratory. Moreover, the rigorous modelling of the experiment involves the numerical solution of the time dependent adjoint equations [35], which is beyond the scope of this publication.

The method adopted to fit the experimental data with the theoretical curves has proved to be effective for evaluating the two fitting parameters, namely the capture coefficients $\alpha_{e,h}$, which are the key parameters used for the characterization of the effects of radiation damage in semiconductors. The capture coefficients depend on: (i) the capture cross-sections $\sigma_{e,h}$, which identify the nature of the recombination centres and (ii) the proportionality factors $k_{e,h}$, which connect the active recombination centres with the concentration of Frenkel pairs introduced as primary point defects. The $k_{e,h}$ factors represent the average number of active defects (carrier recombination centres) corresponding to a single simulated vacancy, and they can be calculated if the intrinsic capture cross-sections $\sigma_{e,h}$ are available from deep level transient spectroscopy [75] or similar techniques based on scanning ion beams [74, 76].

For the study described in this publication, assuming $k_{e,h}$ factors independent of the type of incoming particle [77] and carrier thermal velocities of $v_n^{th} = 2.05 \times 10^7$ cm/s and $v_p^{th} = 1.69 \times 10^7$ cm/s [76], the $k_{e,h}\sigma_{e,h}$ products derived from Eqs (41, 67) are $k_e\sigma_e = 7.8 \times 10^{-17}$ cm^2 and $k_h\sigma_h = 4.8 \times 10^{-16}$ cm^2 for electrons and holes, respectively. If a single acceptor state of divacancy is assumed to be the most abundant electronically active defect in the high purity and low doping n-type silicon created by ion irradiation [7], the capture cross-sections are $\sigma_e = 5 \times 10^{-15}$ cm^{-2} and $\sigma_h = 5 \times 10^{-14}$ cm^{-2} [78] for electrons and holes, respectively. Therefore, the relevant k terms are $k_e \approx 1.6 \times 10^{-2}$ and $k_e \approx 1.0 \times 10^{-2}$ (i.e. about 60 and 100 radiation induced defects are needed to form one stable electron and hole recombination centre, respectively).

However, as highlighted in Ref. [20], these results are strongly dependent on the evaluation of the absolute vacancy profiles, $\eta(x)$. SRIM [16] simulated vacancy profiles have been used for decades to correlate radiation damage to ion beam features (e.g. energy, fluence) and material properties (e.g. composition, structure) for different ion irradiations [79, 80]. SRIM, as well as more elaborate tools such as MARLOWE [44], are based on approximate algorithms (e.g. the binary collision approximation), which usually overestimate the vacancy profile (i.e. the k products are underestimated).

However, these drawbacks do not invalidate the methodology. Assuming that SRIM provides realistic but unnormalized vacancy and ionization profiles, the capture coefficients extracted from the fitting procedure can be considered as reference values, which can be used to compare the radiation hardness of different semiconductor materials or devices and to envisage the corresponding CCE degradation for any ion irradiation and bias condition. An exhaustive

analysis of the connection of these parameters with the nature and the number of stable radiation induced defects requires the use of more elaborate computational tools and experimental techniques and is beyond the scope of this publication.

This report is intended to provide guidance for attaining reliable measurements of the degradation of the CCE, or of any other electronic property of semiconductor devices, induced by displacement damage effects. The proposed methodology overcomes the limitations inherent to the commonly used NIEL approach, which is inferred from a more general model in the case of a constant damage profile, and contributes towards a standardized quantification of the radiation hardness of semiconductor materials.

Appendix I

SUMMARY OF ASSUMPTIONS MADE IN THE MODEL

The assumptions made in the presented analysis and in the determination of the capture coefficients $\alpha_{e,h}$ are as follows:

— Assumption I: Steady state conditions can be applied in the electrostatic description.
— Assumption II: The geometry allows simplification to a one dimensional description.
— Assumption III: The bias voltage V is applied at $x = 0$ and the device is grounded at $x = d$.
— Assumption IV: The electrical contacts are ohmic.
— Assumption V: The device operates in quasi-steady-state conditions (i.e. the excess charge generated does not perturb the electric field significantly).
— Assumption VI: Linearization of the charge generation and recombination terms is valid; namely, the charge generation and recombination terms are linear functions of the charge densities.
— Assumption VII: The recombination centre concentration $N_{e,h}^{Tdam}$ and the concentration of Frenkel pairs created immediately after irradiation, as calculated from binary collision approximation codes such as SRIM [16], are proportional to each other. The Shockley–Read–Hall model is applicable.
— Assumption VIII: The device operates in full depletion conditions.
— Assumption IX: The undamaged device has 100% CCE.
— Assumption X: The DIB fluence as a function of the CCE follows a linear trend (very low level damage).
— Assumption XI: The vacancy profile is constant.

Appendix II

FEATURES OF DEVICE UNDER STUDY 1

Device under study 1 (DUS1) is a commercial silicon photodiode (Hamamatsu S1223). An optical image of DUS1 and its assembly for the measurement are illustrated in Fig. 36. Its main features are described in the datasheet of the supplier [81]. The TO-5 package allows comfortable housing in standard sample holders. The metal can package can be opened by gently sawing or grinding away the can top [54] and removing the borosilicate glass window on top in order to expose the front surface of the photodiode to incident megaelectronvolt energy ions. Since the photodiode is photon sensitive, it is essential to perform all the measurements in dark conditions to avoid the contribution of the photocurrent to the electronic noise.

The extension of the active regions of the device (i.e. the region where the pulse signal is formed) as a function of the applied bias voltage is given by the Gunn weighting potential profiles (see Section 2).

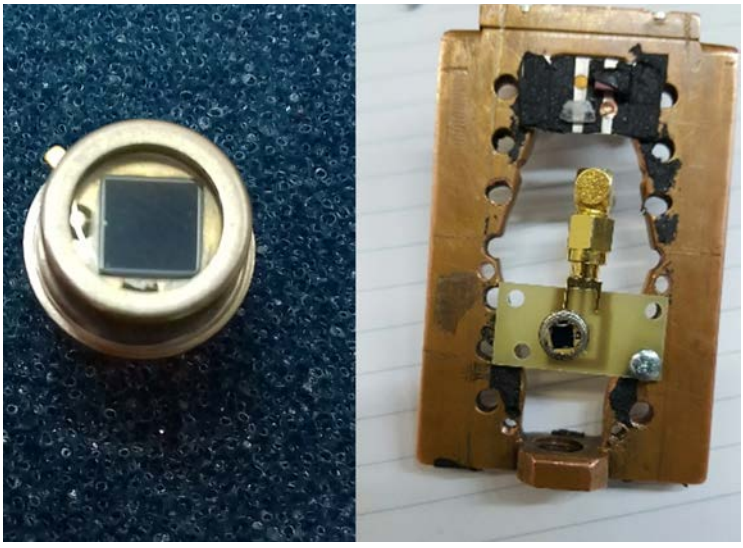

FIG. 36. Left: image of DUS1. Right: housing of the photodiode connected through an SMA connector.

Appendix III

FEATURES OF DEVICE UNDER STUDY 2

The second device, device under study 2 (DUS2), is an n-type float zone silicon detector developed at the Helsinki Institute of Physics. A photograph of this pad detector along with an optical image and a scanning electron micrograph are shown in Fig. 37. It is a p^+–n–p^+ bulk n-type detector with a thickness of 300 μm. The pad area is 5 × 5 mm^2 and the bulk resistivity is 900 Ω · cm. The average n-type doping concentration is 10^{15} cm^{-3}. The device has 17 guard rings; the width of the innermost one is 100 μm and that of the other rings is 16 μm, with a spacing of 10 μm between them. A schematic representation of the device is shown in Fig. 38.

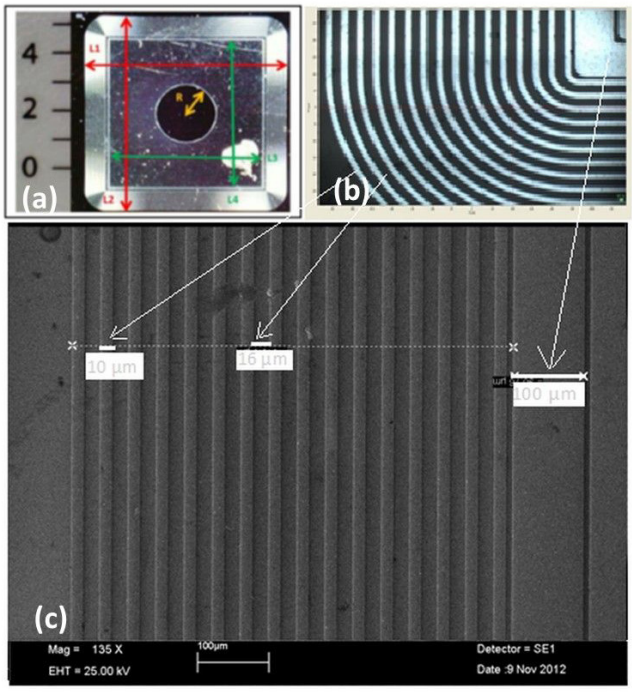

FIG. 37. (a) Photograph of the detector. (b) Optical micrograph of one quadrant of the detector. (c) Scanning electron micrograph of the region of the guard rings. Image reproduced with permission from Ref. [20].

Figure 39 shows the measured capacitance–voltage curve of DUS2 and the depletion width extracted using Eq. (4). The doping profile of the n-type region of DUS2, determined through Eqs (3, 4), is shown in Fig. 40.

A simulation of the electrostatics of DUS2 in steady state conditions, as outlined in Section 2.3, gave the depth dependent profiles of the electron and hole velocities shown in Fig. 41 and the Gunn weighting potential and field depicted in Fig. 42.

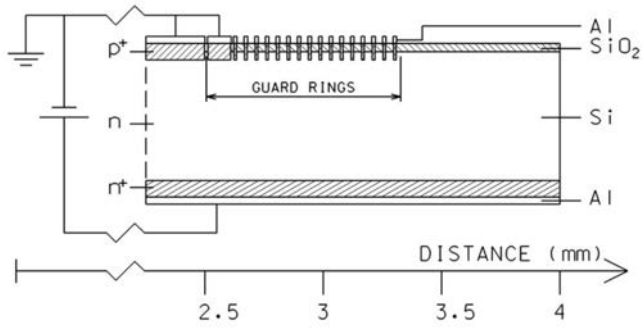

FIG. 38. Cross-sectional view of the edge of DUS2. Figure reproduced with permission from Ref. [82].

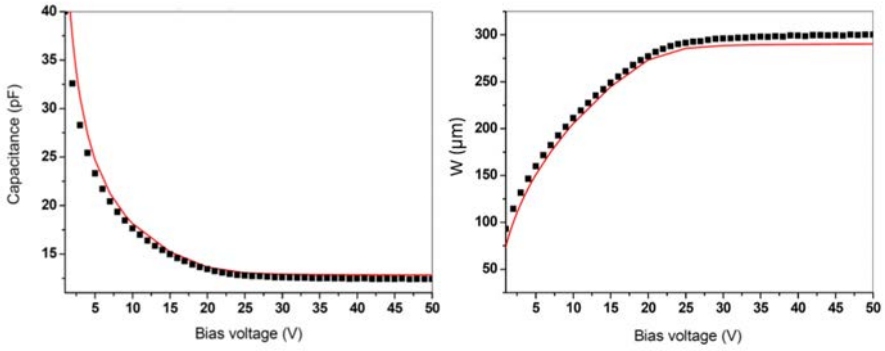

FIG. 39. Left: capacitance–voltage curve of DUS2. Right: depletion layer extension versus bias voltage, calculated from Eq. (4). Figure adapted with permission from Ref. [20].

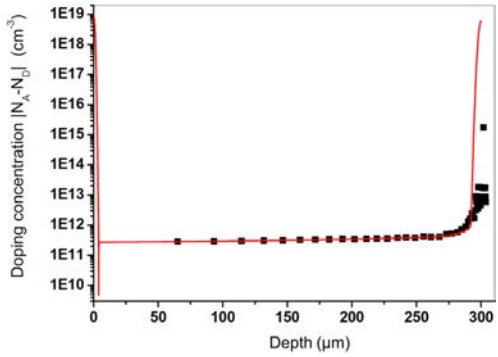

FIG. 40. Doping profile of DUS2 calculated from Eq. (3). Figure adapted with permission from Ref. [20].

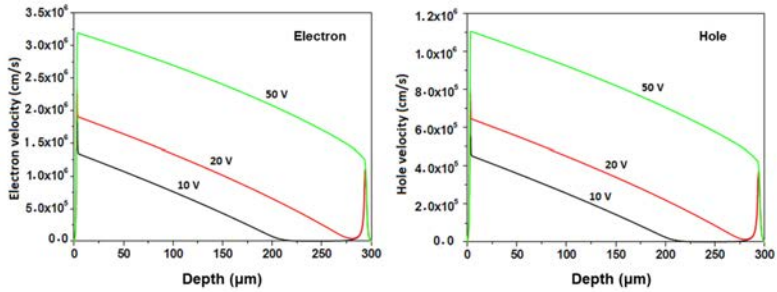

FIG. 41. Electron (left) and hole (right) drift velocity profiles for different bias voltages. Figure adapted with permission from Ref. [20].

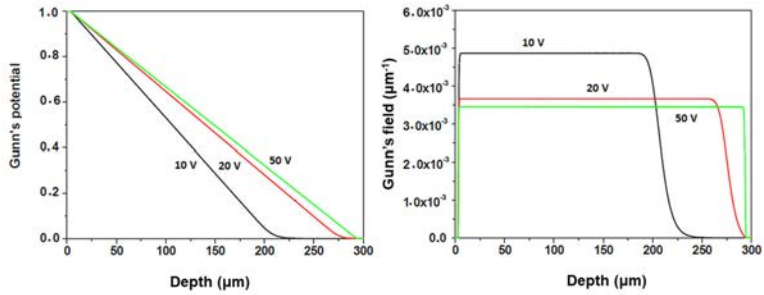

FIG. 42. Gunn weighting potential (left) and Gunn field (right) at different bias voltages. The numbers represent absolute values. Figure adapted with permission from Ref. [20].

Appendix IV

MOBILITY AND LIFETIME PARAMETERIZATION FOR SILICON

The expression describing the mobility in silicon is as follows [26, 27]:

$$\mu_{e,h}(E) = \frac{\mu_{0,e,h}}{\left[1 + \frac{CI}{C_{e,h}^{ref} + \left(CI / S_{e,h}\right)} + \frac{\left(E / A_{e,h}\right)^2}{\left(E / A_{e,h}\right) + F_{e,h}} + \left(\frac{E}{B_{e,h}}\right)^2\right]^{\frac{1}{2}}} \tag{71}$$

where CI is the ionized impurity concentration of the material and the other parameters are summarized in Table 1 [26, 27].

The free carrier lifetime in silicon is also space dependent and is given by the following expression [27]:

$$\begin{cases} \tau_e(x) = \dfrac{N^{ref} \times 3.94 \times 10^{-4}\,\text{s}}{N^{ref} + N_A(x) + N_D(x)} \\ \tau_h(x) = \dfrac{N^{ref} \times 3.94 \times 10^{-5}\,\text{s}}{N^{ref} + N_A(x) + N_D(x)} \end{cases} \tag{72}$$

where $N^{ref} = 7.1 \times 10^3\ \mu m^{-3}$.

TABLE 1. SUMMARY OF PARAMETERS USED IN Eq. (71)

	Electrons (e)	Holes (h)
μ_0	1 400 $cm^2 \cdot V^{-1} \cdot s^{-1}$	480 $cm^2 \cdot V^{-1} \cdot s^{-1}$
$C_{e,h}^{ref}$	$3 \times 10^{16}\ cm^{-3}$	$4 \times 10^{16}\ cm^{-3}$
$S_{e,h}$	350 V/cm	81 V/cm
$A_{e,h}$	3 500	6 100
$F_{e,h}$	8.8	1.6
$B_{e,h}$	7 400 V/cm	25 000 V/cm

Appendix V

DEVICE SIMULATION METHODS AND SOFTWARE

As part of CRP F11016, an IBIC simulation tool was developed by the University of Torino [83][4]. A (non-exhaustive) list of software that may be utilized for the kind of device simulation undertaken here is as follows:

— ATLAS Silvaco[5];
— COMSOL[6];
— SYNOPSYS[7].

Device simulation techniques are powerful tools that can be used in other related spheres to greatly reduce the time and cost involved in the fabrication and testing of prototype devices. Device simulation can be performed through a wide variety of approaches, depending on the complexity, required physical accuracy, application under study and computational demand. In this study, the basic idea is to solve the Poisson and current continuity equations.

For the evaluation of the Gunn potential, the first step is to evaluate the actual potential distribution at a certain bias voltage (e.g. 29.99 V) and then at a slightly different bias voltage (e.g. 30.01 V); the Gunn potential is then calculated as an incremental ratio (i.e. potential at 30.01 V minus the potential at 29.99 V, divided by 0.02 V). The electric field is calculated in a similar fashion. In some device simulation software, there is an option that allows the calculation of the induced charge by directly solving the Maxwell equations.

---

[4] Available at http://www.solid.unito.it/RICERCA/IBA/IST.html
[5] Available at https://www.silvaco.com
[6] Available at https://www.comsol.com
[7] Available at https://www.synopsys.com

REFERENCES

[1] SCHWANK, J.R., SHANEYFELT, M.R., DODD, P.E., Radiation hardness assurance testing of microelectronic devices and integrated circuits: Radiation environments, physical mechanisms, and foundations for hardness assurance, IEEE Trans. Nucl. Sci. **60** 3 (2013) 2074.

[2] MOLL, M., On behalf of the RD50 Collaboration, Development of radiation hard sensors for very high luminosity colliders—CERN-RD50 project, Nucl. Instrum. Methods Phys. Res. A **511** 2 (2003) 97.

[3] RD50 COLLABORATION, Radiation Hard Semiconductor Devices for Very High Luminosity Colliders (2018),
https://rd50.web.cern.ch/rd50/

[4] MESSENGER, S.R., et al., Non ionizing energy loss (NIEL) for heavy ions, IEEE Trans. Nucl. Sci. **46** 6 (1999) 1595.

[5] MESSENGER, S.R., et al., Criteria for identifying radiation resistant semiconductor materials, IEEE Trans. Nucl. Sci. **52** 6 (2005) 2276.

[6] MESSENGER, S.R., et al., Using SRIM to calculate the relative damage coefficients for solar cells. Prog. Photovoltaics **13** 2 (2005) 1062.

[7] PASTUOVIĆ, Ž., et al., Probability of divacancy trap production in silicon diodes exposed to focused ion beam irradiation, Appl. Phys. Lett. **98** 9 (2011) 2.

[8] PASTUOVIĆ, Ž., et al., Ion beam induced charge analysis of radiation damage in silicon photodiodes, Proc. SPIE **8725** (2013) 87251A.

[9] BREESE, M.B.H., VITTONE, E., VIZKELETHY, G., SELLIN, P.J., A review of ion beam induced charge microscopy, Nucl. Instrum. Methods Phys. Res. B **264** 2 (2007) 345.

[10] ZIEGLER, J.F., ZIEGLER, M.D., BIERSACK, J.P., SRIM — The stopping and range of ions in matter, Nucl. Instrum. Methods Phys. Res. B **268** 11–12 (2010) 1818–1823.

[11] VITTONE, E., et al., Semiconductor characterization by scanning ion beam induced charge (IBIC) microscopy, Nucl. Instrum. Methods Phys. Res. B **266** 8 (2008) 1312.

[12] VIZKELETHY, G., Simulation of ion beam induced current in radiation detectors and microelectronic devices, Nucl. Instrum. Methods Phys. Res. B **269** 20 (2011) 2330.

[13] SHOCKLEY, W., READ, W.T., Statistics of the recombination of holes and electrons, Phys. Rev. **87** 5 (1952) 835.

[14] FOLKESTAD, A., et al., Development of a silicon bulk radiation damage model for Sentaurus TCAD, Nucl. Instrum. Methods Phys. Res. A **874** (2017) 94.

[15] ABDEL, N.S., et al., Radiation tolerance of ultra-thin PIN silicon detectors evaluated with a MeV proton microbeam, Nucl. Instrum. Methods Phys. Res. B **356** (2015) 17.

[16] ZIEGLER, J.F., Interactions of ions with matter: SRIM — The stopping range of ions in matter (2013),
http://www.srim.org

[17] SIMON, A., KALONKA, G., Investigation of charge collection in a silicon PIN photodiode, Nucl. Instrum. Methods Phys. Res. B **231** (2005) 507.

[18] PASTUOVIĆ, Ž., et al., Deterioration of electrical and spectroscopic properties of a detector grade silicon photodiode exposed to short range proton, lithium and oxygen ion irradiation, IEEE Trans. Nucl. Sci. **56** 4 (2009) 2457.
[19] VIZKELETHY, G., et al., Investigation of ion beam induced radiation damage in Si PN diodes, Nucl. Instrum. Methods Phys. Res. B **306** (2013) 176.
[20] VITTONE, E., et al., Charge collection efficiency degradation induced by MeV ions in semiconductor devices: Model and experiment, Nucl. Instrum. Methods Phys. Res. B **372** (2016) 128.
[21] PASTUOVIĆ, Ž., et al., Radiation hardness of n-type SiC Schottky barrier diodes irradiated with MeV He ion microbeam, Nucl. Instrum. Methods Phys. Res. B **348** (2015) 233.
[22] LOPEZ, J.G., et al., Comparative study by IBIC of Si and SiC diodes irradiated with high energy protons, Nucl. Instrum. Methods Phys. Res. B **372** (2016) 143.
[23] GRILJ, V., et al., The evaluation of radiation damage parameter for CVD diamond, Nucl. Instrum. Methods Phys. Res. B **372** (2016) 161.
[24] VITTONE, E., SIMON., A. (Eds), Papers arising from IAEA Coordinated Research Project "Utilization of ion accelerators for studying and modelling of radiation induced defects in semiconductors and insulators" (F11016), Nucl. Instrum. Methods Phys. Res. B **372** (2016) 127.
[25] SCHRODER, D.K., Semiconductor Material and Device Characterization, John Wiley & Sons, Hoboken, NJ (1990).
[26] SCHARFETTER, D.L., GUMMEL, H.K., Large signal analysis of a silicon read diode oscillator, IEEE Trans. Electron Devices **16** 1 (1969) 64.
[27] SELBERHERR, S., Analysis and Simulation of Semiconductor Devices, Springer-Verlag, Vienna (1984).
[28] BARRETT, H.H., ESKIN, J.D., BARBER, H.B., Charge-transport in arrays of semiconductor gamma ray detectors, Phys. Rev. Lett. **75** 1 (1995) 156.
[29] PRETTYMAN, T.H., Method for mapping charge pulses in semiconductor radiation detectors, Nucl. Instrum. Methods Phys. Res. A **422** 1–3 (1999) 232.
[30] PRETTYMAN, T.H., Theoretical framework for mapping pulse shapes in semiconductor radiation detectors, Nucl. Instrum. Methods Phys. Res. A **428** 1 (1999) 72.
[31] GUNN, J.B., A general expression for electrostatic induction and its application to semiconductor devices, Solid-State Electron. **7** 10 (1964) 739.
[32] SHOCKLEY, W., Currents to conductors induced by a moving point charge, J. Appl. Phys. **9** 10 (1938) 635.
[33] RAMO, S., Currents induced by electron motion, Proc. IRE **27** 9 (1939) 584.
[34] VITTONE, E., Theory of ion beam induced charge measurement in semiconductor devices based on the Gunn's theorem, Nucl. Instrum. Methods Phys. Res. B **219** (2004) 1043.
[35] MANFREDOTTI, C., et al., Time-resolved ion beam-induced charge collection measurement of minority carrier lifetime in semiconductor power devices by using Gunn's theorem, Mater. Sci. Eng. B **102** 1–3 (2003) 193.
[36] VIZKELETHY, G., Simulation of ion beam induced current in radiation detectors and microelectronic devices, Nucl. Instrum. Methods Phys. Res. B. **269** (2011) 2330.

[37] VITTONE, E., Semiconductor characterization by scanning ion beam induced charge (IBIC) microscopy, ISRN Mater. Sci. 2013 (2013) 637608.
[38] KNOLL, G.F., Radiation Detection and Measurement, 4th edn, John Wiley & Sons, Hoboken, NJ (2010).
[39] FELDMAN, L.C., MAYER, J.W., Fundamentals of Surface and Thin Film Analysis, North-Holland, Amsterdam (1986).
[40] BERNAS, H., Materials Science with Ion Beams, Springer-Vergal, Berlin (2009).
[41] WALLACE, J.B., et al., Radiation defect dynamics studied by pulsed ion beams, Nucl. Instrum. Methods Phys. Res. B. **409** (2017) 347.
[42] SCREENING RELATIVISTIC (SR) NUCLEAR STOPPING POWER CALCULATOR, Screened Relativistic (SR) Treatment for calculating the displacement damage and nuclear stopping powers and doses in materials (version 3.9.3) (2018), http://www.sr-niel.org
[43] NASTASI, M., MAYER, J.W., WANG, Y., Ion Beam Analysis: Fundamentals and Applications, CRC Press, Boca Raton, FL (2014).
[44] ROBINSON, M.T., TORRENS, I.M., Computer simulations of atomic displacement cascades in solids in binary collision approximation, Phys. Rev. B **9** 12 (1974) 5008.
[45] ROBINSON, M.T., Computer simulation studies of high-energy collision cascades in the binary-collision approximation, Phys. Rev. B **67** (1992) 396–400.
[46] PSR-0137 MARLOWE 15B, Computer simulation of atomic collisions in crystalline solids (2018), https://www.oecd-nea.org/tools/abstract/detail/psr-0137
[47] SEITZ, F., Color centers in alkali halide crystals II, Rev. Mod. Phys. **26** 1 (1954) 7.
[48] BERTOLINI, G., COCHE, A., Semiconductor Detectors, North-Holland, Amsterdam (1968).
[49] ORTEC, Preamplifier Introduction (2018), http://www.ortec-online.com/-/media/ametekortec/other/preamplifier-introduction.pdf?la=en
[50] HAMAMATSU SOLID STATE DIVISION, Technical Information SD-37: Characteristic and Use of Charge Amplifier (2001), https://www.hamamatsu.com/resources/pdf/ssd/charge_amp_kacc9001e.pdf
[51] SPEMANN, D., et al., Materials analysis and modification at LIPSION: Present state and future developments, Nucl. Instrum. Methods Phys. Res. B **269** 20 (2011) 2175.
[52] JAKOB, A.M., et al., A characterisation of electronic properties of alkaline texturized polycrystalline silicon solar cells using IBIC, Nucl. Instrum. Methods Phys. Res. B **269** 20 (2011) 2345.
[53] AMPTEK, Charge Sensitive Preamplifier A250 (2018), https://www.amptek.com/internal-products/a250-charge-sensitive-preamplifier
[54] BREESE, M.B.H., JAMIESON, D.N., KING, P.J.C., Materials Analysis Using a Nuclear Microprobe, John Wiley & Sons, Hoboken, NJ (1996).
[55] ORTEC, Introduction to Amplifiers (2018), http://www.ortec-online.com/-/media/ametekortec/other/amplifier-introduction.pdf?la=en

[56] POMMÉ, S., MARROYO, B.C., Improved peak shape fitting in alpha spectra, Appl. Radiat. Isot. **96** (2015) 148.
[57] KLEIN, C.A., Bandgap dependence and related features of radiation ionization energies in semiconductors, J. Appl. Phys. **39** (1968) 2029.
[58] SIEGBAHN, K., (Ed.), Alpha-, Beta- and Gamma-Ray Spectroscopy, North-Holland, Amsterdam (1965).
[59] MARTINI, M., et al., Comparative ionization energies for protons, deuterons and alpha particles in high purity germanium and Si(Li) nuclear radiation detectors, IEEE Trans. Nucl. Sci. **22** 1 (1975) 145.
[60] LO GIUDICE, A., et al., Average energy dissipated by mega-electron-volt hydrogen and helium ions per electron-hole pair generation in 4H-SiC, Appl. Phys. Lett. **87** 22 (2005) 222105.
[61] LO GIUDICE, A., et al., Angle resolved IBIC analysis of 4H-SiC Schottky diodes, Nucl. Instrum. Methods Phys. Res. B **249** (2006) 213.
[62] BREESE, M.B.H., A review of ion beam induced charge microscopy for integrated circuit analysis, Mater. Sci. Eng. B **42** 1–3 (1996) 67.
[63] BOGOVAC, M., et al., Digital pulse processor for ion beam microprobe imaging, Nucl. Instrum. Methods Phys. Res. B **267** 12-13 (2009) 2073.
[64] VIZKELETHY, G., Technical report contribution to the final report of the IAEA CRP 11016 on "Utilization of ion accelerators for studying and modelling of radiation induced defects in semiconductors and insulators", IAEA, Vienna (2016).
[65] CORBETT, J.W., WATKINS, G.D., Production of divacancies by electron irradiation of silicon, Phys. Rev. **138** 2A (1965) A555.
[66] BARBERO, N., et al., Degradation of the charge collection efficiency of an n-type Fz silicon diode subjected to MeV proton irradiation, Nucl. Instrum. Methods Phys. Res. B. **348** (2015) 260.
[67] BREESE, M.B.H., GRIME, G.W., WATT, F., Study of nuclear microprobe halo using IBIC, Nucl. Instrum. Methods Phys. Res. B **77** 1–4 (1993) 243.
[68] DOYLE, B.L., VIZKELETHY, G., WALSH, D.S., Ion beam induced charge collection (IBICC) studies of cadmium zinc telluride (CZT) radiation detectors, Nucl. Instrum. Methods Phys. Res. B **161** (2000) 457.
[69] ASTM INTERNATIONAL, Standard Practice for Ensuring Test Consistency in Neutron-Induced Displacement Damage of Electronic Parts, Standard ASTM E1854-07, ASTM International (2007).
[70] COMSOL, Multiphysics Modelling and Simulation, ver. 3.5. (2018), www.comsol.com
[71] NIST, Digital Library of Mathematical Functions (2017), http://dlmf.nist.gov/
[72] BRANDT, S., Statistical and Computational Methods in Data Analysis, 3rd edn, North-Holland, Amsterdam (1978).
[73] JAMES, F., MINUIT Function Minimization and Error Analysis: Reference Manual Version 94.1 (1994), http://inspirehep.net/record/1258343?ln=it

[74] KADA, W., et al., Development of diagnostic method for deep levels in semiconductors using charge induced by heavy ion microbeams, Nucl. Instrum. Methods Phys. Res. B **348** (2015) 240.
[75] LANG, D.V., Deep level transient spectroscopy: New method to characterize traps in semiconductors, Bull. Am. Phys. Soc. **19** 3 (1974) 298.
[76] LAIRD, J.S., et al., Scanning ion deep level transient spectroscopy, Nucl. Instrum. Methods Phys. Res. B **158** 1–4 (1999) 464.
[77] LEROY, C., RANCOITA, P.G., Particle interaction and displacement damage in silicon devices operated in radiation environments, Rep. Prog. Phys. **70** 4 (2007) 493.
[78] VINES, L., et al., Effect of spatial defect distribution on the electrical behavior of prominent vacancy point defects in swift-ion implanted Si, Phys. Rev. B **79** 7 (2009) 1.
[79] UZAN-SAGUY, C., et al., Damage threshold for ion-beam induced graphitization of diamond, Appl. Phys. Lett. **67** (1995) 1194.
[80] LOHSTROH, A., et al., Ion beam induced charge (IBIC) irradiation damage study in synthetic single crystal diamond using 2.6 MeV protons, Phys. Status Solidi A **205** (9) (2008) 2211.
[81] HAMAMATSU, Si PIN Photodiodes S1223 series (2013), http://www.hamamatsu.com/resources/pdf/ssd/s1223_series_kpin1050e.pdf
[82] VÄYRYNEN, S., RÄISÄNEN, J., KASSAMAKOV, I., TUOMINEN, E., Breakdown of silicon particle detectors under proton irradiation, J. Appl. Phys. **106** (2009) 104914.
[83] FORNERIS, J., JAKŠIĆ, M., PASTUOVIĆ, Ž., VITTONE, E., A Monte Carlo software for the 1-dimensional simulation of IBIC experiments, Nucl. Instrum. Methods Phys. Res. B **332** (2014) 257–260.

SYMBOLS

A	area of the electrodes (i.e. active area)
$\alpha_{\mathrm{e,h}}$	electron (e) and hole (h) capture coefficient
C	capacitance
c	capacitance per area
D	active thickness
D_{d}	displacement damage dose
$D_{\mathrm{e,h}}$	electron (e) and hole (h) diffusion coefficient
d	device thickness
$-\frac{\mathrm{d}E}{\mathrm{d}x}$	linear stopping power
$\frac{\mathrm{d}E_{\mathrm{ion}}}{\mathrm{d}x}$	specific ionization energy loss
$\left(-\frac{\mathrm{d}E}{\mathrm{d}x}\right)_{\mathrm{electronic}}$	electronic stopping power
$\left(-\frac{\mathrm{d}E}{\mathrm{d}x}\right)_{\mathrm{nuclear}}$	nuclear stopping power
$\boldsymbol{E}$	electric field
$\boldsymbol{E}^{+}$	Gunn weighting field
E_{ion}	ion energy
E_{loss}	energy loss
E_{trans}	energy transferred by an ion in one collision
ε	dielectric permittivity

ε_{ehp}	average energy dissipated by ionization radiation per electron–hole pair generation
ε_{Vac}	average energy to produce a vacancy
$f_{e,h}$	electron (e) and hole (h) normalized quasi-Fermi level
$f^{+}_{e,h}$	Gunn electron (e) and hole (h) normalized quasi-Fermi level
Φ	ion fluence
Φ^{*}	effective damaging ion beam fluence
φ	electrostatic potential
φ^{+}	Gunn weighting potential
φ_{th}	thermal potential (at room temperature)
φ_{N}	normalized potential
$G_{e,h}$	electron (e) and hole (h) generation term in the continuity equation
$G^{+}_{e,h}$	electron (e) and hole (h) adjoint generation term
$\Gamma(x)$	electron–hole pair generation profile
$\gamma(x)$	normalized electron–hole pair generation profile
$\boldsymbol{H}$	Hessian matrix
$\eta(x)$	vacancy distribution
$J_{e,h}$	electron (e) and hole (h) current density
$K_{e,h}$	recombination (lifetime) damage coefficient for electrons (e) and holes (h)

K_{ed}	equivalent damage factor
k_B	Boltzmann constant
$k_{e,h}$	average number of active defects (carrier recombination centres) generated by a single vacancy
$\boldsymbol{M}$	matrix of the sum of the squares of the residuals normalized by the uncertainty $\sigma(i)$ of the ith measurement
m_e	electron mass
m_{ion}	ion mass
$\mu_{e,h}$	electron (e) and hole (h) mobility
N_A	ionized acceptor concentration
N_D	ionized donor concentration
$N_{e,h}^{T*}$	density of recombination centres for electrons (e) and holes (h)
$N_{e,h}^{T0}$	density of recombination centres for electrons (e) and holes (h) before ion irradiation
$N_{e,h}^{Tdam}$	density of recombination centres for electrons (e) and holes (h) created by the ion irradiation
n_0	thermal equilibrium electron density
n^+	adjoint electron concentration
p_0^+	adjoint electron concentration at time $t = 0$
n_i	intrinsic carrier concentration
p	free hole concentration
p_0	hole density at thermal equilibrium

p^+	adjoint hole concentration
n_0^+	adjoint hole concentration at $t = 0$
Q	charge induced at the sensing electrode
$Q_{\mathrm{e,h}}$	charge induced at the sensing electrode due to electron (e) and hole (h) motion
$Q^*(\theta)$	free charge generated by the incident ion under varying incidence angle θ
q	elementary charge
q_{T}	total space charge within the depletion region
$R_{\mathrm{e,h}}$	electron (e) and hole (h) recombination term in the continuity equation
R^{d}	maximum depth of vacancy profile when approximated by Eq. (57)
ρ_{M}	mass density
$\sigma(i)$	uncertainty in the ith measurement
$\sigma_{\mathrm{e,h}}$	electron (e) and hole (h) capture cross-section
$\sigma_{\mathrm{e,h}}^{\mathrm{dam}}$	electron (e) and hole (h) capture cross-section of the damage induced traps
T	temperature
t	time
t^*	dead layer thickness
$\tau_{\mathrm{e,h}}$	electron (e) and hole (h) lifetime
$\tau_{\mathrm{e,h}}^0$	electron (e) and hole (h) lifetime (undamaged material)

$\tau_{e,h}^{dam}$	electron (e) and hole (h) lifetime component due to ion induced damage
Θ	Heaviside step function
θ	incidence angle
V	applied bias voltage
V_{bi}	built-in potential
V_{tot}	total number of vacancies
$\boldsymbol{v}_e$	electron rift velocity
$\boldsymbol{v}_h$	electron drift velocity
$\boldsymbol{v}_{e,h}^{th}$	electron (e) and hole (h) thermal velocities
W	extension of the depletion layer

ABBREVIATIONS

CCE	charge collection efficiency
CRP	coordinated research project
DIB	damaging ion beam
DUS1	device under study 1
DUS2	device under study 2
IBIC	ion beam induced charge
PIB	probing ion beam
SRIM	Stopping Range of Ions in Matter

CONTRIBUTORS TO DRAFTING AND REVIEW

Garcia Lopez, J.	Centro Nacional de Aceleradores, University of Sevilla, Spain
Grilj, V.	Ruđer Bošković Institute, Croatia
Jakšić, M.	Ruđer Bošković Institute, Croatia
Jimenez Ramos, C.	Centro Nacional de Aceleradores, University of Sevilla, Spain
Lohstroh, A.	University of Surrey, United Kingdom
Pastuović, Ž.	Australian Nuclear Science and Technology Organisation, Australia
Rath, S.	University of Delhi, India
Siegele, R.	Australian Nuclear Science and Technology Organisation, Australia
Simon, A.	International Atomic Energy Agency
Skukan, S.	Ruđer Bošković Institute, Croatia
Vittone, E.	University of Torino, Italy
Vizkelethy, G.	Sandia National Laboratories, United States of America

IAEA
International Atomic Energy Agency

No. 26

ORDERING LOCALLY

IAEA priced publications may be purchased from the sources listed below or from major local booksellers.

Orders for unpriced publications should be made directly to the IAEA. The contact details are given at the end of this list.

NORTH AMERICA

Bernan / Rowman & Littlefield
15250 NBN Way, Blue Ridge Summit, PA 17214, USA
Telephone: +1 800 462 6420 • Fax: +1 800 338 4550
Email: orders@rowman.com • Web site: www.rowman.com/bernan

REST OF WORLD

Please contact your preferred local supplier, or our lead distributor:

Eurospan Group
Gray's Inn House
127 Clerkenwell Road
London EC1R 5DB
United Kingdom

Trade orders and enquiries:
Telephone: +44 (0)176 760 4972 • Fax: +44 (0)176 760 1640
Email: eurospan@turpin-distribution.com

Individual orders:
www.eurospanbookstore.com/iaea

For further information:
Telephone: +44 (0)207 240 0856 • Fax: +44 (0)207 379 0609
Email: info@eurospangroup.com • Web site: www.eurospangroup.com

Orders for both priced and unpriced publications may be addressed directly to:

Marketing and Sales Unit
International Atomic Energy Agency
Vienna International Centre, PO Box 100, 1400 Vienna, Austria
Telephone: +43 1 2600 22529 or 22530 • Fax: +43 1 26007 22529
Email: sales.publications@iaea.org • Web site: www.iaea.org/publications

The operational useful lifetime of semiconductor electronic devices working in harsh radiation environments is limited by the structural defects induced by exposure to ionizing radiation. This has immediate consequences for their use in high radiation environments, for example in nuclear facilities, satellites, radiotherapy, medical diagnostics, security and other industries. This publication establishes a standardized procedure to quantify the radiation hardness of semiconductor devices in a way that is independent of the irradiation parameters and biasing conditions of the device. The established parameters reflect the cross-sections of additional free charge carrier trapping induced by the damaging radiation, normalized to the predicted concentration of vacancies generated by the same radiation. The effectiveness of the approach is validated through different types of ion beam irradiation, characterizations and materials used. The work leads towards approaches to predict radiation induced effects on device performance for more complex electronic structures.

INTERNATIONAL ATOMIC ENERGY AGENCY
VIENNA